12-2005

A Microreactor System for Measuring Size Selectivity in Porous WO3 Sensor Materials

Meng Lu

A MICROREACTOR SYSTEM FOR MEASURING SIZE SELECTIVITY IN POROUS WO_3 SENSOR MATERIALS

By

Meng Lu

B.S. Tianjin University, 1999

A THESIS

Submitted in Partial Fulfillment of the

Requirements for the Degree of

Master of Science

(in Chemistry)

The Graduate School

The University of Maine

December, 2005

Advisory Committee:

Brian G. Frederick, Associate Professor of Chemistry, Advisor

M. Clayton Wheeler, Assistant Professor of Chemical Engineering

François G. Amar, Associate Professor of Chemistry

Carl P. Tripp, Professor of Chemistry

Robert J. Lad, Professor of Physics

A MICROREACTOR SYSTEM FOR MEASURING SIZE SELECTIVITY IN POROUS WO_3 SENSOR MATERIALS

By Meng Lu

Thesis Advisor: Dr. Brian G. Frederick

An Abstract of the Thesis Presented
in Partial Fulfillment of the Requirements for the
Degree of Master of Science
(in Chemistry)
December, 2005

Our interest in studying reactions catalyzed by high surface area WO_3 powders is based on their potential application as the active material in sensors for low level (ppb) detection of flammable or toxic gases. A series of porous WO_3 powders with both meso- and micro-porosity have been synthesized by Waghe and Tripp. Preliminary results of the response of sensors fabricated from these materials indicated the possibility of size selectivity on the molecular scale. To provide support for the hypothesis of size selectivity and understand the reaction kinetics of alcohols over the new porous WO_3 powders for sensor applications, we have designed and verified a new microreactor system to measure the product distribution, reaction rates (activity), and influence of transport through nanoscale and mesocopic pores.

This microreactor system is composed of three parts, a quantitative gas source, a

microreactor for powder materials, and a GC/MS for quantitative analysis of reactant and product concentrations. A detailed account of the design parameters and rationale of the experimental facility are presented, and a quantitative analysis of the uncertainties in the concentration measurements is also shown in this work. Before we started the alcohol oxidation experiments, the system was calibrated, and the instrumental method was optimized. According to the quantitative analysis, the relative uncertainty in concentrations was about 6%, consistent with the design.

The oxidation reactions of a series of alcohols (methanol, ethanol, 2-propanol, 2-butanol and 2-hexanol) over Al_2O_3 (pure Denstone support media), nonporous WO_3/Al_2O_3 and porous WO_3/Al_2O_3 were studied. The product distributions and alcohol conversion as a function of temperature were measured. Dehydration and dehydrogenation products were observed as the main alcohol oxidation products. However, trace amounts of aldol condensation products were also detected in some alcohol oxidation reactions, and the presence of these condensation products was related to the potential effect of water on the alcohol oxidation. Reaction kinetic analysis of 2-butanol on nonporous and porous WO_3 suggested a potential effect of the pore size of WO_3 to selectivity.

ACKNOWLEDGEMENTS

First of all, I wish to express my deep and sincere appreciation to my advisor, Dr. Brian G. Frederick for his guidance, assistance and encouragement during my study in University of Maine. I thank Dr. Carl P. Tripp for supplying the nonporous and porous WO_3 powders samples. I thank Dr. M. Clayton Wheeler for offering important help to me when I doing the pressure drop calculation and reactor model determination. I thank John Monnier, who gave us a lot of valuable suggestions about the system design. I thank Eric Martin for his guidance on the machining of VLEs and Dr. Zhongyu Yang for his help on the MS trouble shooting. I also thank all my committee members for their comments on this thesis.

Special thanks go to my girl friend Li Tao for her love and encouragement.

TABLE OF CONTENTS

LIST OF TABLES

LIST OF FIGURES

Chapter 1

INTRODUCTION

1.1 SMO Sensor Materials

In the early 1960's, it was well known that the electrical properties of semiconducting metal oxides (SMO) vary with the composition of the gases in the surrounding atmosphere[1-3]. These properties have induced wide investigation of their potential application as gas sensors over the past 40 years.

The first oxide to be studied extensively was ZnO[1]. A SnO_2 based sensor was developed and commercialized by Taguchi[4] in the 1960's, which was applied primarily in Japan to detect and warn of explosive methane gas. Potentially effective sensor materials for methanol detection could be materials that have shown good activity as catalysts, as reported by Taylor et al.[5] and Hutchings et al.[6], including Ga_2O_3, MoO_3, Nb_2O_5, Ta_2O_5 and WO_3. Mixed metal oxides are also being studied in both commercial and research sectors. For example, the two component oxide Ga_2O_3/MoO_3 has been studied as a methanol oxidation catalyst[5].

Metal oxide sensors are typically fabricated as a thin film oxide layer or as a powder anchored using a suitable binder to an underlying platform containing the electrical contacts. For metal oxide sensors to be successfully commercialized there are several significant factors: sensitivity, response time, selectivity and reproducibility of the sensor. At the material properties level, factors including the size of grains in the sensing film or powder, grain boundaries and other defect structures, the thickness of the film, and

dopants can be very important for sensor performance. Both thin film and high surface area powder materials have advantages and disadvantages.

By using thin film techniques[7-10], sensor materials can be easily fabricated. Thin films grown epitaxially on a single crystal substrate, can be characterized in great detail and allow tremendous insight into the mechanism of surface reactions. The fabrication of high quality thin film materials may provide opportunities to tailor the surfaces for a specific reaction by controlling the surface structures. However, for practical use in SMO sensors, the two major issues that must be resolved are selectivity and response time. Some effort has been made to use specific surface chemistries to respond selectively to a particular class of compounds[11]. Another approach is to use an array of sensors with pattern recognition software to distinguish classes of compounds[12, 13]. Studies have shown that the sensor response could be improved by using films composed of nanosized particles or doping with transition metals[1, 14, 15]. For instance, Au or Ag has been deposited on WO_3 films to improve the sensor response to NO in our group[16, 17]With recent developments in nanotechnology, it may be possible to utilize the "lock and key" approach that has been prevalent in biology for some time as a means of achieving molecular-scale recognition.

There are advantages and disadvantages of high surface area materials. First, the high surface area allows spectroscopic measurements to be made with IR, Raman, NMR, and other techniques with good sensitivity under more realistic conditions than in UHV studies. Second, the dimensions of the oxide structural elements in the zeolite-like cage

structures can be several nanometers, greatly reducing the response time due to oxygen vacancy diffusion in the "bulk" of the material. Third, the material apparently can be annealed in a way by which the pore dimensions can be collapsed to produce pores of molecular dimensions. Such pores then have the potential to distinguish molecules of different size.

The major disadvantage of these materials is the greater complexity, and therefore difficulty, in characterizing the structure. Some information regarding the meso and nano-scale structure can be obtained from BET adsorption isotherms and high resolution TEM; to the extent that the material is crystalline, X-ray diffraction can provide structural information; spectroscopic measurements, particularly with probe molecules, can elucidate the acidity of surface sites, which may be related to surface activity[18].

1.2. Motivation for This Thesis

Our interest in studying reactions catalyzed by high surface area WO_3 powders is based on their potential application as the active material in sensors for low level (ppb) detection of flammable or toxic gases[11, 17, 19-21]. Typically, the sensors will be operated in an atmospheric pressure, gaseous environment that contains a complex mixture of compounds. Under these conditions it is difficult to decipher the complicated molecular chemistry that leads to a change in conductivity in semiconducting metal oxide based sensors. Therefore, the ability to quantify the transport processes under atmospheric pressure conditions, identify surface species and reaction products formed on the WO_3

surface and determine which factors control the sensor response would certainly aid the development of this sensor technology. WO_3 is a promising sensor material and it has been used as the sensing element in detection of nitric oxides[16, 17], H_2S[22] and organophosphonate[11, 23]. Knowledge of surface reactivity of the WO_3 surface is a key factor to explore its potential sensor applications. The properties of the crystalline WO_3 have been studied in detail, including its semiconductivity and production of oxygen vacancies and crystallographic shear planes[24, 25].

Recently, a series of porous WO_3 powders with both meso- and micro-porosity have been synthesized by Waghe[18], using cationic surfactant based recipes as templating molecules. Preliminary results of the response of sensors fabricated from these materials have suggested a route to achieve selectivity between methanol and DMMP (dimethyl methyl phosphonate), indicating the possibility of size selectivity on the molecular scale.

Table 1.1 shows the BET surface area and d-spacing of several WO_3 powders synthesized in Tripp's group[18]. Although the information about the pore size of porous WO_3 was supposed to be gained by evaluating the N_2 adsorption and desorption branches of type IV isotherms, the exact pore size distribution was not shown in Waghe's[18] study because of instrumental limitations (see N_2 adsorption experiments in Chapter 3 (section 3.3.5) of Waghe's thesis). However, IR measurements[18] with alcohols show the strongest evidence that the pore size is on the molecular scale and can distinguish methanol from large alcohols. Sensors fabricated from these porous WO_3 materials have been used to detect a series of alcohols and DMMP, which is a commonly

used surrogate for nerve agents. The sensors were stabilized with zero air flow to establish a baseline, and then they were tested against a series of random pulses of the alcohols and DMMP with a minimum of three separate pulses per alcohol. DMMP pulses were performed after alcohols because DMMP would poison the sensor. The conductivity change (ΔC), which was the difference between the pulse conductivity and baseline conductivity, was calculated for each pulse. The experimental results are shown in Figure 1.1, where $\Delta C_{mesoporous}/\Delta C_{nonporous}$ is the ratio of the conductivity change obtained on each mesoporous WO_3 sensor to that of the nonporous WO_3 sensor. Figure 1.1 shows that the $\Delta C_{mesoporous}/\Delta C_{nonporous}$ for methanol is about 0.8 and for DMMP this value is 0.2 for both porous materials. The difference in magnitude indicates that the large molecules are not able to diffuse into the material and so the conductivity is modified only on a small fraction of the material at the external surfaces of the powder material.

Table 1.1. BET surface area and d-spacing of porous WO_3 samples

Sample	Type	XRD 2θ	d Å	Surface area m^2/g
A1	MCM-41	7.32	12.0	120
A2	MCM-41	13.2	6.71	112
A3	MCM-41	20.6	4.31	98

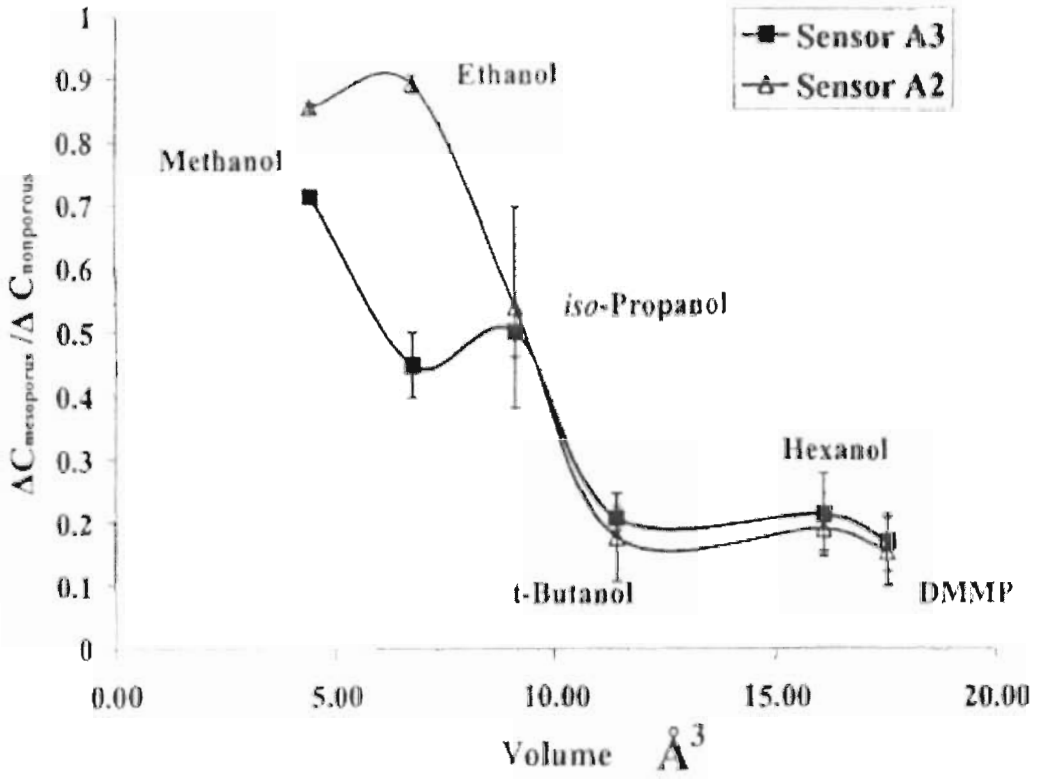

Figure1.1. $\Delta C_{mesoporous}/\Delta C_{nonporous}$ value as a function of size of the molecules.

(From ref. 18, used with permission)

Not only as a means of providing support for the hypothesis of size selectivity, but also to reach a point in which a model can be used to establish the optimal conditions, it is necessary to have an understanding of the roles of the transport and surface reaction processes under realistic conditions. Therefore, our initial goal was to design a

microreactor system to measure the product distribution, reaction rates (activity), and influence of transport through nanoscale and mesoscopic pores. The results would then allow the development of a model to characterize the limits of achievable selectivity.

Alcohol oxidation on nonporous and porous WO_3 was be studied by means of the new microreactor system. Methanol, ethanol, 2-propanol, 2-butanol and 2-hexanol were chosen as the reactants because: 1) these alcohols have been widely used as probe molecules in catalysis and surface science; and 2) these alcohols have similar molecular sizes (Figure 1.2.) to the target compounds in Waghe's studies[18]. The shape and size of the alcohol molecule were obtained using van der Waals radii in the program ChemDraw.

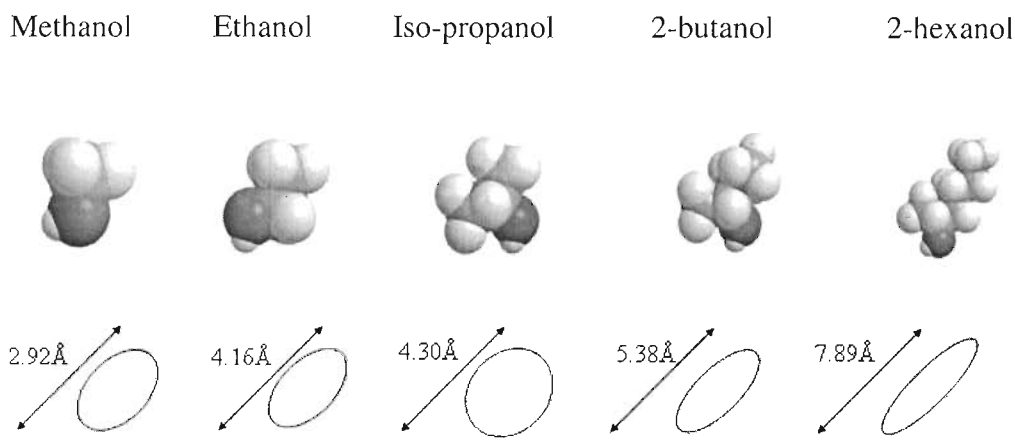

Figure 1.2. Space filling models of various alcohols showing relative sizes and shapes.

1.3 Reactions of Alcohols on WO_3

The adsorption and reaction of alcohols on metal oxide catalysts has been used as a chemical probe reaction for many years. For instance, methanol was reported as a

"smart" chemical probe molecule[26] in studying the metal oxide catalytic activity; 2-propanol[27] and 2-butanol[28] have also been taken as an effective probe to study the acid and base properties of metal oxides.

Alcohol reactions on WO_3 can be generally divided into two pathways: (1) reactions of oxidation that need oxygen and (2) reactions of dehydration that do not need oxygen. Studies showed that the products of alcohol reactions were strongly correlated with the acidic character of WO_3[26-29]. In this thesis, "alcohol oxidation" is used to describe the alcohol reactions on WO_3, which refers to a network of oxidation/dehydration reactions as described in the review by Tatibouët[29].

The reaction mechanisms of several alcohols, ethers, and organophosphonates on WO_3 surfaces have been studied in the past several years in our group[23, 30, 31] under UHV conditions to understand the decomposition mechanisms that fundamentally control the information that can be extracted from the time-dependent response of semiconducting metal oxide sensors. In parallel, testing of thin film, epitaxially grown WO_3 sensors under atmospheric conditions to low concentrations (ppb to ppm levels) of target and interferent gases have been performed[11, 17, 21] on microfabricated sensors[7, 10, 32] developed at the Laboratory for Surface Science and Technology (LASST). The results compare favorably to the response of WO_3 powder sensors fabricated on the same platforms[32], suggesting that the surface chemistry on the epitaxial films is very similar to the powder materials[33], which have been investigated extensively with infrared and Raman techniques[34-37].

1.4. Turnover Frequency (TOF)

To make a comparison of the activity of nonporous and porous WO_3 conveniently and straightforwardly, we employed the turnover frequency (TOF) in the process of kinetic analysis. TOF, which is typically defined as the number of molecules converted per second per active surface metal oxide site[38], is a convenient factor to describe the catalytic activity in the phenomenon of catalysis. When the number of active surface sites is known, the TOF can be specified quantitatively. However, sometimes it is difficult to determine the number of active surface sites in heterogeneous catalysis. For these cases, active surface sites are often replaced by the total surface area, which is readily measurable. Expressions for TOF in terms of the unit mass or unit of volume of catalyst are also applied. Although the IUPAC (International Union of Pure and Applied Chemistry) recommends TOF to be expressed per unit surface area, TOF expressed per unit time is most frequently used in publications. Since TOF is used to describe the reaction rate, it is necessary to specify all of the prevailing conditions of the reaction. For most heterogeneous reactions involving the transformation of small molecules in the temperature range 100-500°C and pressure of up to a few bars, the magnitude of the TOF is between 10^{-2} and $10^{2}s^{-1}$.[38]

1.5. Fixed Bed Reactor Model

In our experiments, the microreactor was designed as a fixed bed reactor, where the catalyst bed was composed of Denstone support media and nonporous or porous WO_3

powders. Fixed bed reactors[27-29, 39] were often used to study alcohol oxidation on WO_3. For the gas-solid reaction in the fixed bed reactor, the detailed process is shown in Figure 1.3. The process can also be separated into three parts: reactant transport to the surface (processes 1 and 2); surface reaction (processes 3, 4 and 5); product transport out of the surface (processes 6 and 7).

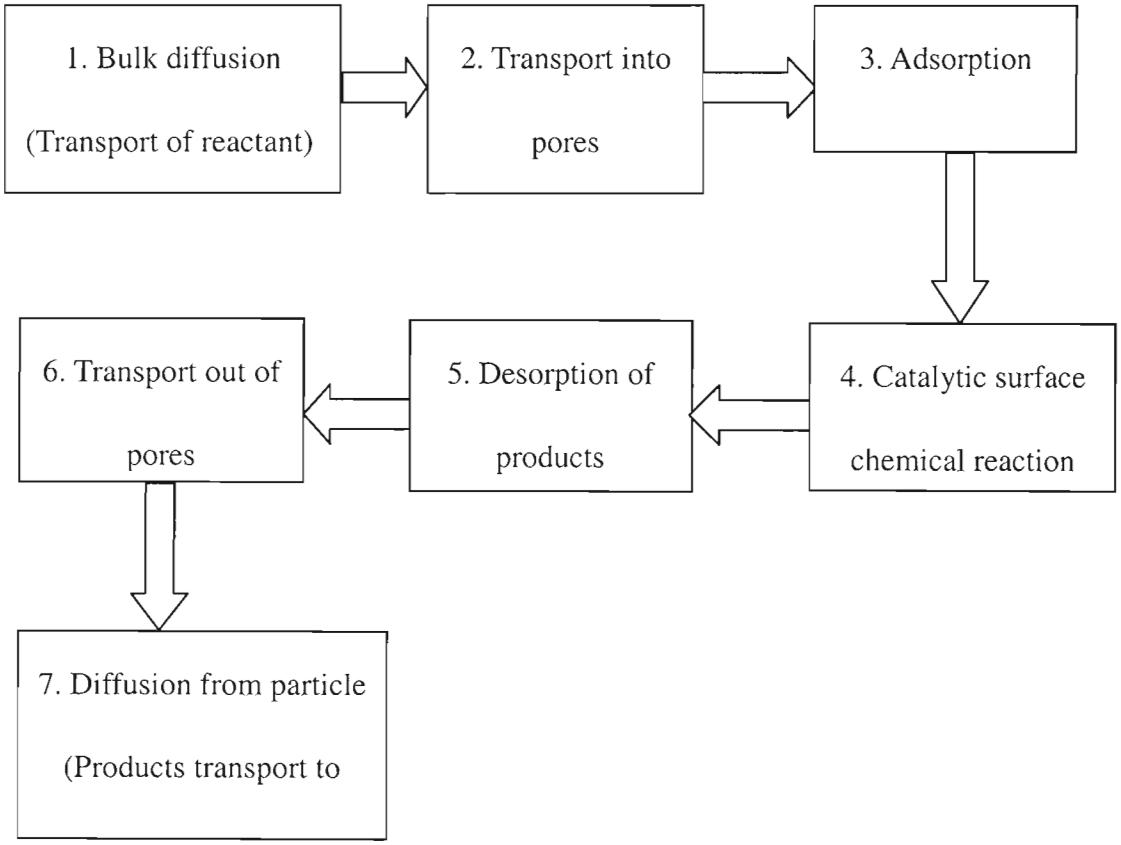

Figure 1.3. Gas-solid reaction process in a fixed bed reactor model.

Alcohol oxidation reactions on WO_3 powders in a fixed bed reactor can be illuminated by employing the process mentioned above. Assuming that alcohol oxidation is irreversible and the product diffusion (6 and 7) is ignored, understanding the process of reactant transport to the surface and into the pores (processes 1 and 2) and surface reactions (processes 3, 4 and 5) is vital in studying the kinetics of alcohol oxidation. The process of reactant transport to the surface can be expressed by:

$$R_{trans}=k_m a_m(c_b-c_s) \qquad (1)$$

where R_{trans} is the transport rate; k_m is the mass transfer coefficient; a_m is the total catalyst area, c_b is the concentration of methanol in the (bulk) carrier gas stream and c_s is the concentration of methanol on the surface. The surface reaction process (assuming a first order reaction) can also be expressed by:

$$R_{rxn}=kc_s \qquad (2)$$

where R_{rxn} is the reaction rate and k is the rate coefficient for the reaction. At steady state, R_{trns} is equal to R_{rxn} and c_s can be expressed by:

$$c_s=(k_m a_m c_b)/(k+k_m a_m) \qquad (3)$$

The overall reaction rate becomes:

$$\begin{aligned} R_{overall} &= R_{rxn} \\ &= kc_s \\ &= (kk_m a_m c_b)/(k+k_m a_m) \\ &= c_b/(1/k+1/k_m a_m) \end{aligned} \qquad (4)$$

There are two limiting cases that give a simple interpretation of the overall rate. When

$R_{rxn} << R_{trans}$ ($k << k_m$), the expression of $R_{overall}$ changes to:

$$R_{overall} = kc_b \qquad (5)$$

which means the rate limited process is the surface reaction. If $R_{rxn} >> R_{trans}$ ($k >> k_m$), the expression of $R_{overall}$ becomes:

$$R_{overall} = k_m a_m c_b \qquad (6)$$

which means the alcohol oxidation is a mass transfer limited reaction. In the limiting cases, the kinetic analysis of alcohol oxidation on WO_3 can be simplified to a great extent.

1.6. Organization of the Thesis

The remainder of the thesis is as follows. In Chapter 2 we describe the design of the microreactor system and experimental procedure, while calibration and an analysis of the performance of the system are given in Chapter 3. In Chapter 4 we reported the product distribution and conversion of each alcohol over nonporous and porous WO_3 powders. The possible size selectivity was demonstrated by analyzing 2-butanol dehydration over nonporous and porous WO_3 catalysts at 100 and 200°C. Chapter 5 presents a summary of the results of this work and suggestions for further progress toward instrument method modification, water effect confirmation, and sensor research.

Chapter 2

EXPERIMENTAL

Two main aspects of the experimental details are presented in this chapter: one is the design of the microreactor system, which consisted of a gas delivery system, a microreactor, and a quantitative analysis system based on GC/MS (gas chromatography / mass spectrometry); the other is the experimental procedure. Some important experimental parameters, including the particle sizes of packing materials, flow rates of target compounds, and reaction temperatures, are also presented in detail.

2.1 System Design

A schematic diagram of the entire system is shown in Figure 2.1. We will describe first the design of the gas delivery section, second the microreactor, and third the GC/MS based quantitative analysis component of the system.

2.1.1. A Quantitative Gas Delivery System Design

In this system, Vapor Liquid Equilibrators (VLEs) are introduced to generate known concentrations of liquid reactants in the feed stream. In the VLE, the target compound is in the liquid phase, and the carrier gas is fed into the VLE and saturated with vapor by bubbling through the liquid. By appropriately choosing the ratio of both carrier gas flow as well as the temperature of the VLE, a flow of carrier gas with various degrees of saturation can be generated reproducibly. Compared with our previous method of

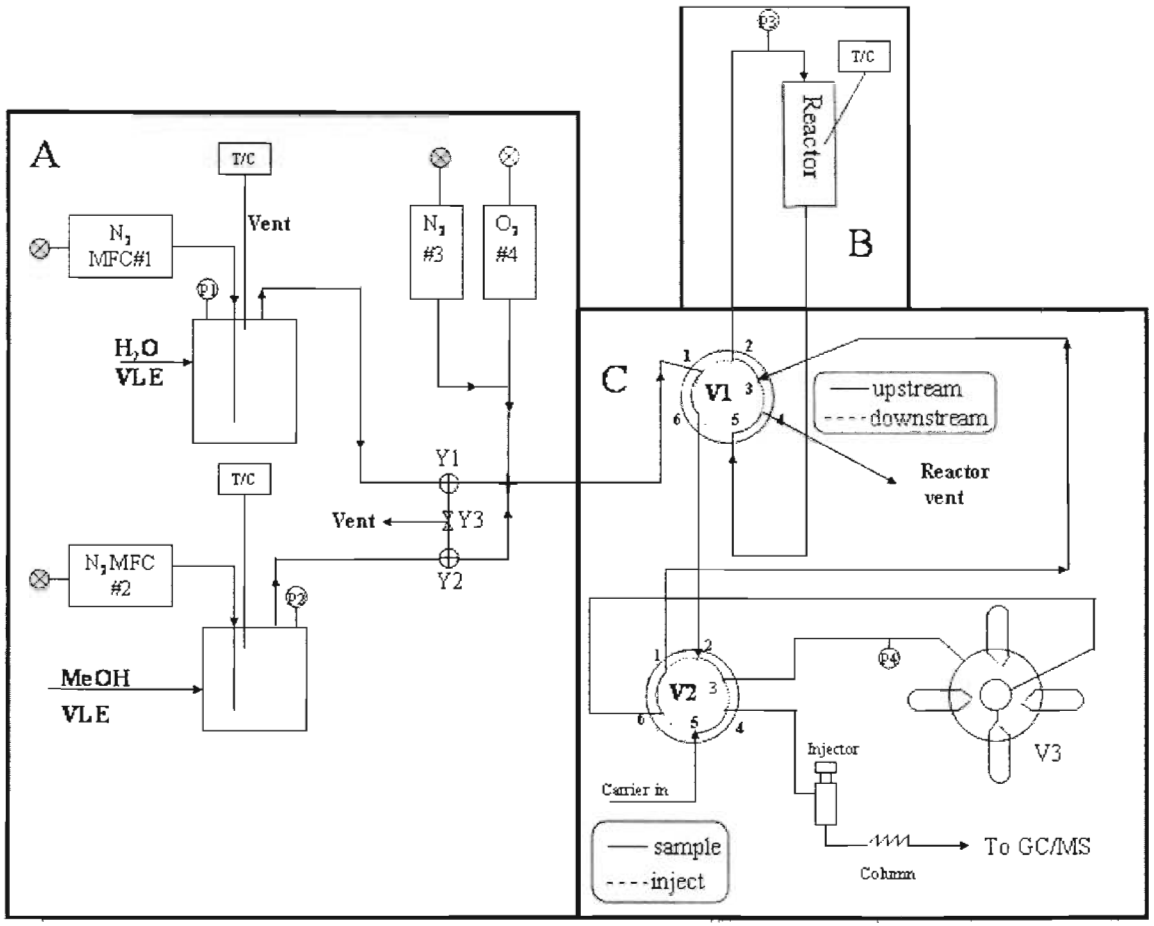

Figure 2.1. Schematic diagram of microreactor system (A: gas delivery system, B: microreactor; C: GC/MS-based quantitative analysis system).

preparing pressurized cylinders containing the target gas mixture[11], VLEs have advantages of greater accuracy (can be better than 1%, compared to about 10% with our previous methods), if designed and operated correctly. Permeation sources are equally accurate; however, VLE's have the advantage of the ability to change quickly from one compound to another (the lead time to order permeation cells is typically 4-6 weeks), particularly if the experiment requires many different compounds. Both permeation sources and VLE's, however, require individual ovens or regulated temperature baths to control the reactant concentration and a calibrated mass flow controller (MFC) for the carrier gas.

The VLEs consist of a container of the liquid compound, held at constant temperature, with sufficient headspace that the vapor remains in thermal equilibrium with the liquid. The structure of a VLE is shown in Figure 2.2. The VLEs were made of 304 stainless steel tubing and two stainless steel lids. The tubing was 2.552 inches long, with an OD of 2.000" and an ID of 1.900" to achieve an internal volume of approximately 100 ml. With 60 ml of liquid, the headspace is 40 ml, and with a carrier gas flow of up to 40 sccm, the average residence time of gas in the headspace is at least one minute, which is usually sufficient to ensure good mixing of the gases prior to exiting the device. The top lid has four 1/4" NPT holes, into which NPT to 1/8" Swagelok connectors can be inserted. This allows the connectors to be replaced easily if damaged and larger openings for cleaning the VLEs to use again for different compounds. The lip on the edge of the bottom lid was designed similarly to the weld

groove on the top, but provides alignment during the welding process. The four ports are used for 1) the carrier gas inlet, which runs through a tube to the bottom of the liquid; 2) the gas stream outlet; 3) a thermocouple (*Omega, KMTSS-040(G)-12*) to measure the liquid temperature to within 2.2°C; and 4) a stainless steel 0-14 psi standard pressure gauge (*Mathesontrigas, 63-2215*) to measure the pressure in the headspace region. The

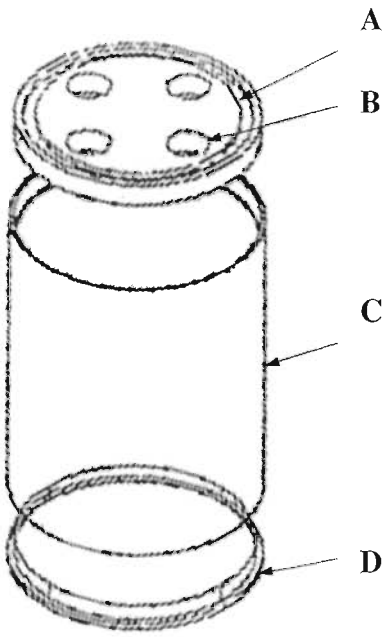

Figure 2.2. Exploded view of VLE. A: Groove, OD 1.8000", ID 1.600"; B: four 1/4" NPT tapped holes, one for pressure gauge, one for thermocouple, and the other two for carrier gas inlet and gas stream outlet separately; C: 304 SS tubing, length 2.522", OD 2.000", ID 1.900"; D: lid, thickness 0.187", diameter 1.930".

gauge accuracy in factory specification was 0.15 psi, however our calibration experiments indicated that the uncertainty was larger by a factor of 2 - 4 (see section 3.8).

Returning to Figure 2.1, both valves Y1 and Y2 are manual, three-way, valves (*Swagelok, SS-41XS2*) used either to vent the gas stream during pre-exposure equilibration, or to switch the gas into the reactor feedstream. Mass flow controllers (*Tylan, FC-2901V*) MFC1, 2, and 3 are calibrated for N_2 carrier gas, and their flow ranges are 0-100 sccm and 0-1000 sccm and 0-100 sccm, respectively. Using Ar for the carrier gas in the reactant VLE (MFC2) would allow both the response time of the delivery system and the microreactor bed to be determined. MFC4 (*Tylan, FC-260, 0-100 sccm*) was designed to allow the partial pressure of O_2 to be varied, although in these experiments synthetic air (see section 2.2.2)was supplied to all the MFC's. Varying the oxygen partial pressure could affect the substoichiometry of the WO_3 and would also allow us to investigate the dependence of the rate laws on p_{O_2}. The N_2 and O_2 (MFC3 and 4) could be adjusted to make up the total gas flow to a constant flow (typically 200-500 sccm). Note that the effluent from the VLEs should enter the gas manifold as close as possible to the valve V1 to reduce cross contamination of the condensable liquid; the distance from the valves Y1 and Y2 to the high velocity carrier gas stream should be minimized. We actually reduced the distance to about 2.5" by using a union cross (*Swagelok, ss-200-4*), where the three inlets for the carrier gas and the target gases combine into the outlet gas mixture. Because of the big pressure difference between the

VLE head space and the microreactor when Y1 or Y2 were changed from vent mode to feed mode, the needle valve Y3 (*Swagelok, SS-20VS4*) was added to the system to protect the MFCs and reduce the reactor response time (see section 3.4.). All the tubing used to connect the VLEs and reactor was 1/8in Sulfinert tubing (*Restek, 22506)*, which was chosen to provide an unreactive pathway for the carrier gas and target compound.

2.1.2. Microreactor Design

The design of the microreactor is shown schematically in Figure 2.3. We used 1/4" chemically inert stainless steel tubing (Sulfinert tubing, *Restek, 22507*) as the reactor wall. Three 4" long brass collars (OD: 1") were bored through and cut into two pieces from the midline. Six bolts were used for each brass collar to achieve a tight fit to the stainless steel tubing. Glass wool plugs were used to hold the catalyst, which was nonporous or porous WO_3 dispersed in crushed and sieved Denstone support (*Saint-Gobain, Denstone 99 support spheres, 1/8"*). Because the sphere size was too big for the reactor, the Denstone support needed to be crushed to get smaller particle sizes, and the actual packing parameters for the Denstone support and WO_3 are presented in section 2.2.2. Two thermocouples (*Omega, JMTSS-040(*)-12*) were used to measure the temperatures of the brass collar and the inside of the reactor; the pressure gauge P3 (*Mathesontrigas, 63-2215*) was used to measure the pressure upstream of the catalyst bed, mainly for safety purposes. To allow the temperature profile along the reactor bed to be measured, a thermowell was constructed, into which the thermocouple (sheath

2.1.3. GC/MS Based Quantitative Analysis System

The quantitative analysis system, shown schematically in section C of Figure 2.1, was designed to allow the reactant stream to be sampled upstream of the reactor as well as the product stream to be measured downstream of the reactor. Conversion of the reactant could be acquired by analyzing the MS response of these two cases mentioned above. Additionally, from the known concentrations of reactant gases (see section 3 below), the mass spectrometer signal could be calibrated to about 5% accuracy (see section 3.7.).

The heart of the sampling system consists of two six-port, two-position valves, V1 (*VICI, A26UWT*) and V2 (*VICI, A6C6UWT*), and a 16-loop sampling valve V3 (*VICI, E25ST16P*). When V1 is in the upstream mode (ports are connected by solid lines, see Figure 2.4.), the reactant gas goes first to the sampling valve (V3), before passing to the reactor (i.e. the gas is sampled upstream of the reactor); while if V1 is switched to the downstream position (dashed lines, see Figure 2.5.), then the gas first passes through the reactor and then to the sampling valve. In either case, the stream always passes through the reactor in the direction indicated. If V2 is in the sampling position (solid line), the gas passes through one of the 16 loops of V3. Rotation of V3 traps a gas sample, which is then stored for subsequent analysis. When V2 is in the inject position (dashed lines), then the carrier gas pushes the gas sample in the engaged loop of V3 onto the GC column. Rotation of V3 then injects subsequent gas samples stored in consecutive loops. The loop capacity, i.e. the number of moles of reactant in the loop, was calculated from the volume

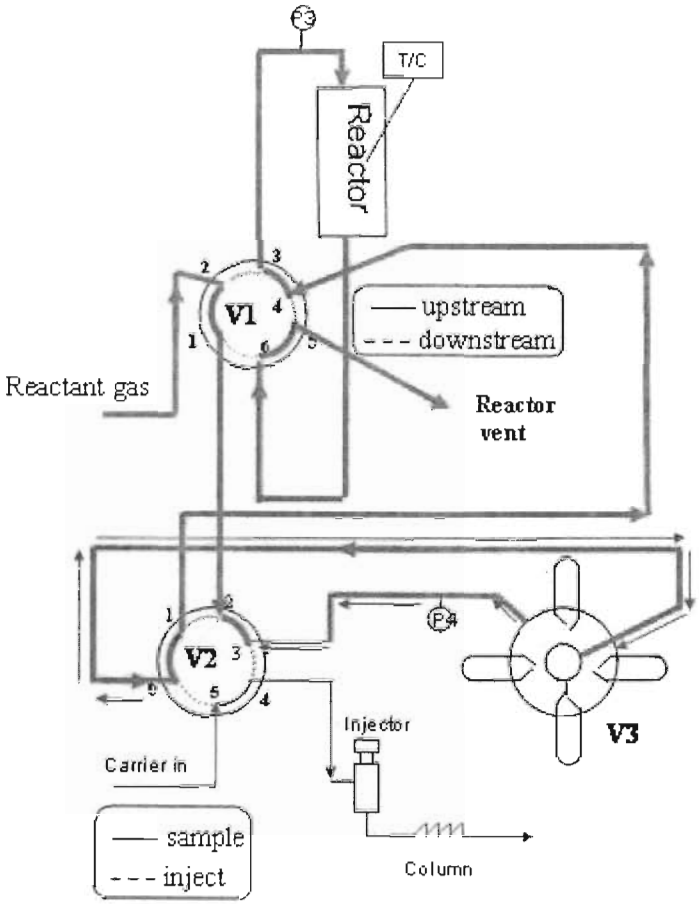

Figure 2.4. Sampling in upstream mode.

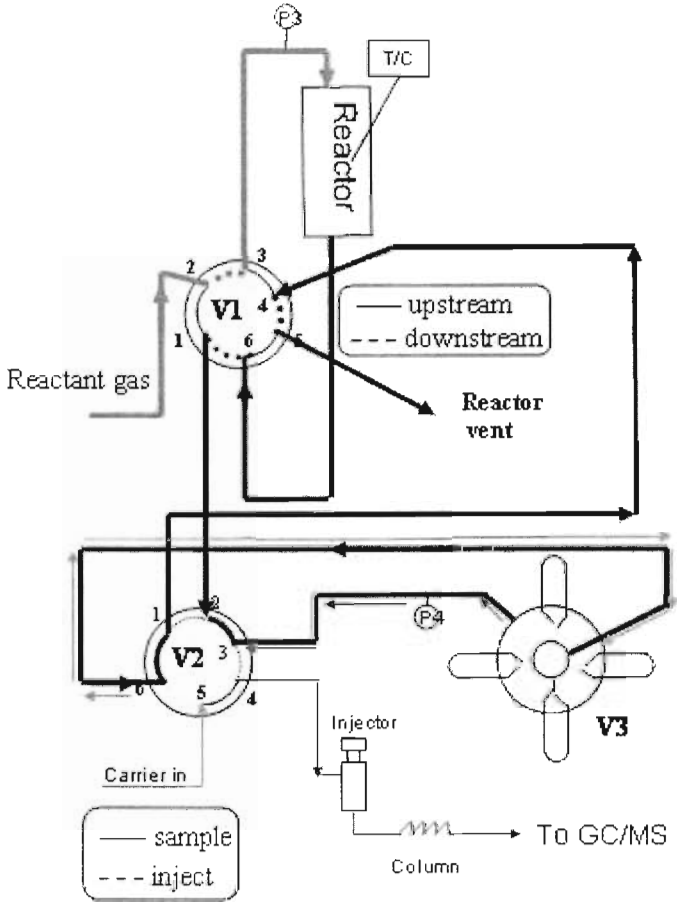

Figure 2.5. Sampling in downtream mode.

and measured pressure, which was monitored by the test gauge P4 (*Mathesontrigas, 63-5615M*) with 0.035psi measurement uncertainty. The GC/MS (*Finnigan, Trace™ GC 2000 and Trace MS*) was used with a DB-1 capillary column (*J&W Scientific Inc., 122-1033*) to separate alcohols and selective oxidation products. However, CO and CO_2 could not be separated from the air by using the DB-1 column.

2.1.4. Operating Procedures of the Microreactor System

The typical operating procedures used to operate this system can be described as follows:

1) Calibration experiments

For each temperature and packing sequence, the reactant is delivered to the GC before passing through the reactor (see Figure 2.4). The MS sensitivity to the reactant can be deduced through quantitative analysis. The calibration experiments can also be used to measure the volume reproducibility of the 16 sampling loops. To check that the reactant has reached equilibrium in the headspace of the VLE, measurements of the reactant as a function of flow through the VLE (but constant dilution) should be independent of the VLE flow. The linearity of the system should also be tested by measuring the MS signal versus dilution.

2) Blank experiments

The blank experiments are used to measure the catalytic activity of the Denstone to the reactant and correct the conversion of the reactant when changed with catalyst. For

low temperature (no reaction, but adsorption could occur) and up to high reaction temperature, the reactant is delivered to the GC after passing through the microreactor (see Figure 2.5) with only pure Denstone support in the reactor.

3) Pre-conditioning experiments

Exposing the sample to carrier gas prior to switching the reactant can be done to pre-condition the catalyst (as typically done during calcination and reduction cycles on metal supported catalysts, for example). In this work, the catalyst was allowed to reach steady state in the reactant stream because we were more concerned with steady state conditions than transient behavior.

4) Reaction kinetic measurements

The reactant is delivered to the GC after passing through the reactor at a particular temperature (see Figure 2.5). The catalyst bed in the reactor includes the Denstone support and the WO_3 catalyst. Information about the reactant conversion and product distribution can be gained.

5) Product calibration experiments

To quantify the activity for a particular product or the selectivity of the product distribution, MS sensitivity factors for each of the products need to be measured (as in step 1).

2.2. Experimental Procedure

2.2.1. Microreactor Packing

Denstone support media was manually crushed into powders, and then sieved by using fine test sieves (*Sigma-Aldrich*) with size 25 mesh, 40 mesh, 80 mesh, and 170 mesh in sequence. First of all, glass wool was inserted into the top of the reactor to prevent Denstone support media from sliding into the inlet tubing; then, according to the reactor pressure drop calculation (see section 3.5.1.), Denstone media with different particle size and nonporous (*Aldrich, 204781-1*) or porous WO_3 (A2 sample) were packed into the reactor from top to bottom by inverting the reactor; at last, glass wool was inserted into the bottom of the reactor to support the catalyst. The packing parameters for different experiments are shown in Table 2.1.

Table 2.1. Microreactor packing parameters for different experiments (Packing sequence in the reactor: left to right correspond to from the top down).

	Denstone (710-425μm)	WO_3 powder	Denstone (180-90μm)	Denstone (425-180μm)	Denstone (710-425μm)
Denstone and nonporous WO_3 (A2)	2500mg	250mg nonporous (~20μm)	250mg	500mg	1500mg
Denstone and porous WO_3	2500mg	50mg porous (≤25μm)	250mg	500mg	1500mg
Pure Denstone	2500mg	N/a	250mg	500mg	1500mg

2.2.2. Measurement Procedures

Both N_2 and O_2 flows (see Figure 3.1) were replaced by compressed air flow generated by a Zero Air Generator (*Parker Balston, 76-803*), which made the N_2/O_2 flow ratio in the total stream about 4:1 and provided gas purity below 0.05 ppm (part per million) total hydrocarbon content. Helium (Grade 5.0) was used as the carrier gas in the GC/MS. A series of alcohols, methanol (*Fisher, A452-4*), ethanol (*Acros, 61509-0020*), 2-propanol (*Fisher, A416-4*), 2-butanol (*Sigma-Aldrich, 19440-250ML*), and 2-hexanol (*Sigma-Aldrich, 128570-100G*) were used as the target samples. The water VLE was filled with about 60ml deionized water.

MFC4 was removed from the system because MFC3 was supplied by the Zero Air Generator. The specific flow rates of MFC1, MFC2 and MFC3 for different experiments are shown in Table 2.2. Concentrations of the alcohols were calculated as shown in **Appendix A** and the Antoine coefficients are given in **Appendix B**. A series of experiments with different microreactor temperatures (Room temperature, 100°C, 200°C, 250°C, 300°C, 350°C, and 400°C) have been run for each target sample. For each experiment, the 16 sampling loops of valve 3 were loaded within 50 minutes. The first 8 sampling loops of V3 were loaded in up-stream mode, and the other 8 sampling loops were loaded in the downstream mode. The specific sample loading time and GC operating conditions will be presented later in section 3.6.

Table 2.2. Set point flow rates of the MFC's for different experiments.

Packed materials	Reactant	MFC1 (sccm)	MFC2 (sccm)	MFC3 (sccm)	Total (sccm)
Denstone and nonporous WO_3	Methanol Ethanol 2-propanol 2-butanol	40	5	200	245
	2-hexanol	40	10	200	250
Denstone and porous WO_3	Methanol Ethanol 2-propanol	40	10	200	250
	2-butanol 2-hexanol	40	10	100	150
Pure Denstone	Methanol Ethanol 2-propanol 2-butanol	40	5	200	245
	2-hexanol	40	10	200	250

The separation of the compounds was carried out with the following GC oven temperature program: isothermal at -15°C for 3.5 min, a temperature increase of 50°C/min up to 50°C and hold at this temperature for 2 min (see section 3.6.1.). The quadrupole mass spectrometer conditions were: electron energy, 70 eV; emission current, 320 μA; ion source temperature, 200°C; detector voltage, 350 V; ionization mode, electron impact (EI+) (see section 3.7.). Mass spectra were recorded by full scanning from 13 to 90 mass units with the sampling setting selected in the Xcalibur software (GC peak width, 4 seconds; minimum scan per GC peak, 10). Identification of the compounds was carried out by comparison of the detected mass spectra with the NIST mass spectral library and gas chromatography data base[40].

Chapter 3

CALIBRATION AND ERROR ANALYSIS

Temperature, flow rate and pressure are very important parameters in the semi-quantitative analysis performed in our experiments, and the concentration uncertainty of the target compound in the sampling loop also depends on the uncertainties of these parameters to a great extent. To get a better accuracy, the temperature controller, pressure gauges and MFC's were calibrated at the beginning of the experiments. The specific calibration processes, as well as the determination of the actual experimental conditions (e.g. microreactor packing, GC and MS operating conditions), are discussed and presented. Because of the significant effect of pressure on gas phase reactions, the pressure drop, due to pathway tubing, the microreactor itself, and the valves, is estimated to better quantify the alcohol reaction rates. At the end of this chapter, a quantitative analysis of the target compounds is shown in detail.

3.1. Temperature Calibration

The microreactor was heated to different temperatures with a heat tape which was connected to the temperature controller (*Omega, CN76000*). The standard K type thermocouple (*Omega*) for the temperature controller was put just outside the brass collar and packed with the heat tape. During the test experiments of methanol on Al_2O_3/nonporous WO_3 (Denstone and nonporous WO3), we noticed that the temperature shown in the display panel of the temperature controller was different from the internal

thermowell temperature which was measured with a digital voltmeter (*Cen-tech, P37772*). The relationship between these two temperatures is shown in Figure 3.1. To understand the temperature difference, we changed the methanol flow to pure carrier gas flow (synthetic air), but we still got almost the same relationship of these two temperatures. Therefore, we concluded that the exothermic alcohol oxidation reactions did not contribute too much to the big temperature difference (~20°C). We also repacked the thermocouple inside the heat tape and found the temperature difference changed dramatically (±10°C). Hereby, the temperature difference was mainly caused by the poor thermal contact between the thermocouple and the brass collar.

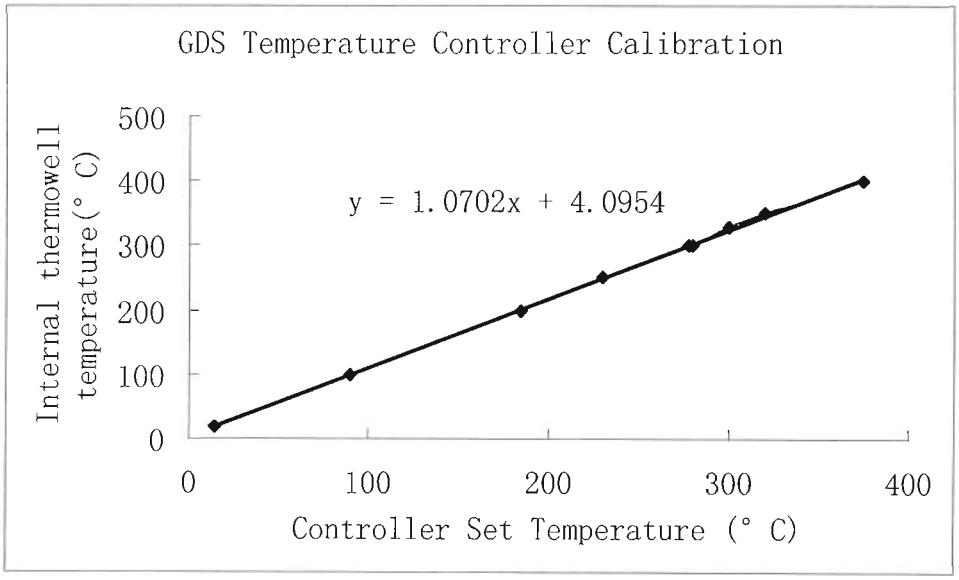

Figure 3.1. The relationship between thermowell temperature and temperature controller set temperature. (For methanol oxidation on Al_2O_3/WO_3, MFC1=40 sccm, MFC2=5 sccm, MFC3=200 sccm).

The thermowell temperatures at different positions are shown in Figure 3.2. The thermowell position was labeled from the top of the microreactor to bottom (0 to 25cm). The catalyst bed (Denstone and nonporous WO_3) was located between 5 and 19cm, and the position of WO_3 powder relative to the thermowell was about 12cm. From Figure 3.2 we can see that the thermowell temperature in the range of the catalyst bed was almost constant at each specific set temperature.

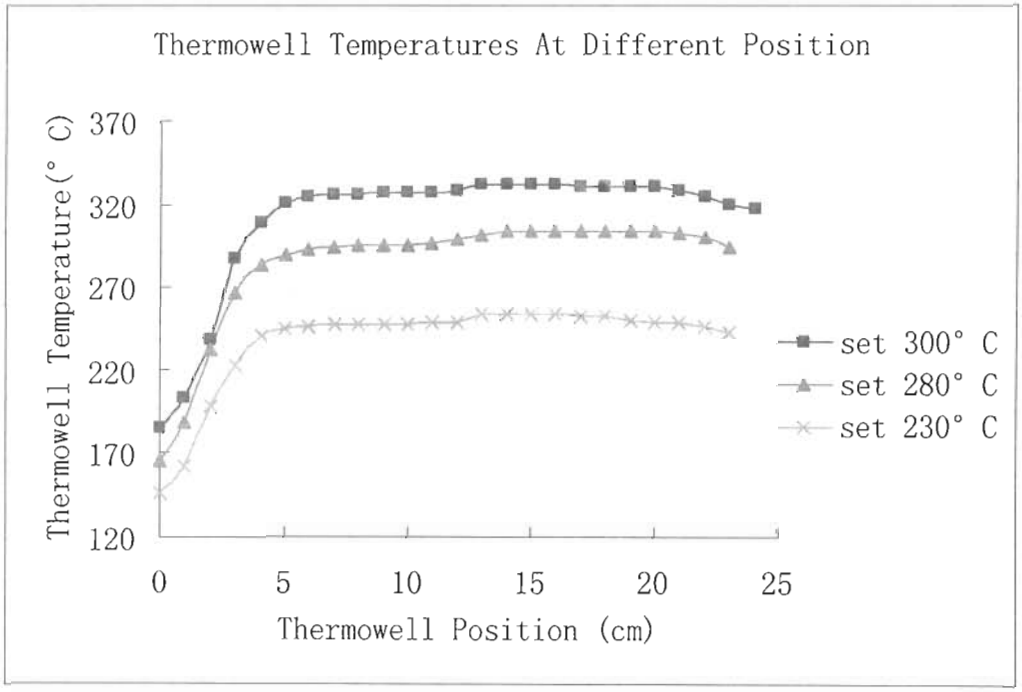

Figure 3.2. Thermowell temperature profiles with different controller set temperatures. (For methanol oxidation on Al_2O_3/WO_3, MFC1=40 sccm, MFC2=5 sccm, MFC3=200 sccm).

3.2. MFC Calibration

Poor performance by an MFC can affect the validity of the measurements in at least two ways. Irreproducibility of the MFC limits the accuracy of the system, and inaccuracy of the MFC will give errors in the measurements of activity that would be important for transferring knowledge gained in these experiments to actual sensor work. All the MFC's used in our experiments have been pre-calibrated in N_2 by the factory. However, the carrier gas we planned to use was purified air, and the MFC's left unused for a long time might be inaccurate or damaged. The MFC's should be recalibrated to get a good performance.

MFC1, 2 and 3 were calibrated by using a soap bubble method (see Figure 3.3.). Purified air generated by the Zero Air Generator flowed through the MFC and into a tee at the base of a 50ml buret. The rubber bulb was filled with a soap solution so that bubbles could be produced. A soap film (a bubble) could be made by squeezing the rubber bulb. This soap film traveled up the buret as gas flowed through the MFC. The gas flow could be measured by monitoring the change in position of the soap film with time (i.e. the time for the soap film to travel, e.g. to the 1ml, 10ml, or 50ml volume marker on the buret tube.) The actual flow rate was the change in volume divided by time.

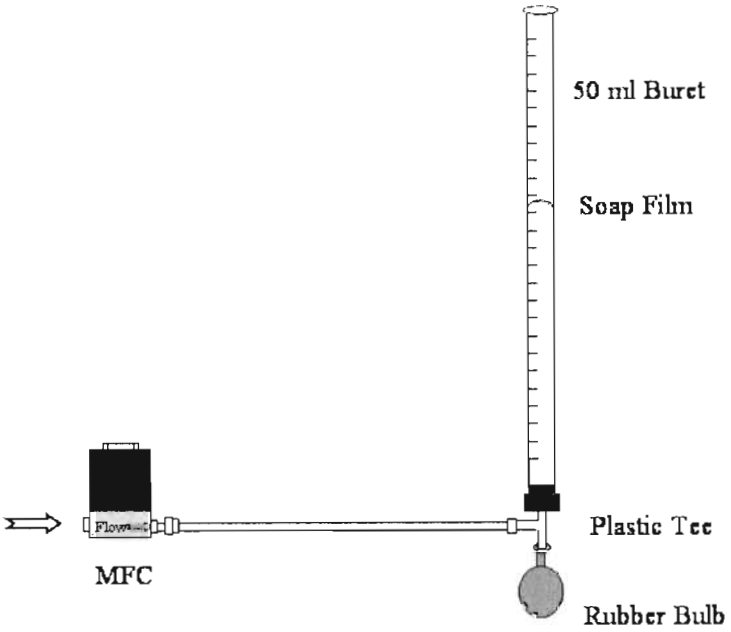

Figure 3.3. Schematic illustration of soap bubble method.

By changing the MFC set point flow rates, the MFC calibration curves were made (see Figures 3.4-3.6.). The values of the MFC calibrations and their uncertainties, which will be used for statistical analysis (see section 3.8.), are listed in Table 3.1.

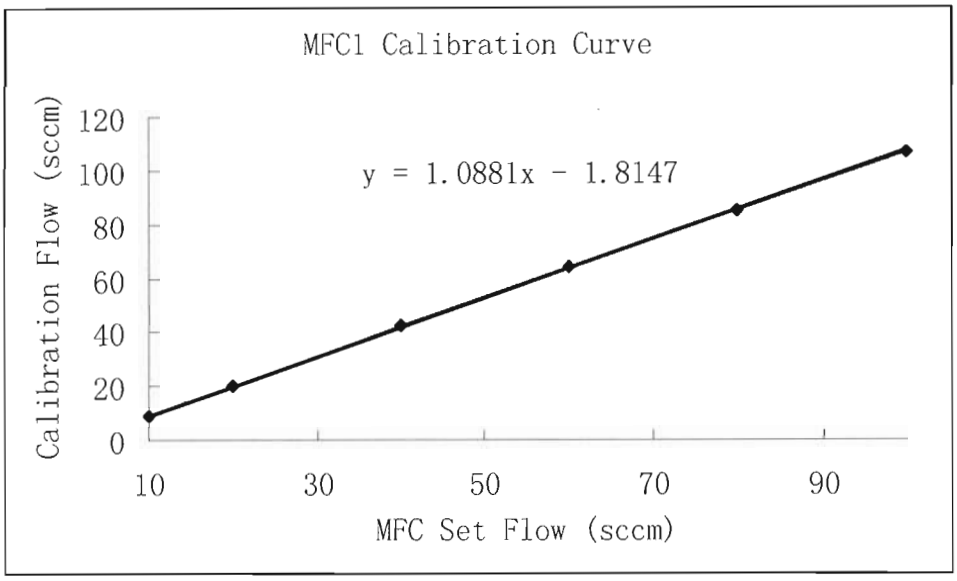

Figure 3.4. MFC1 Calibration Curve.

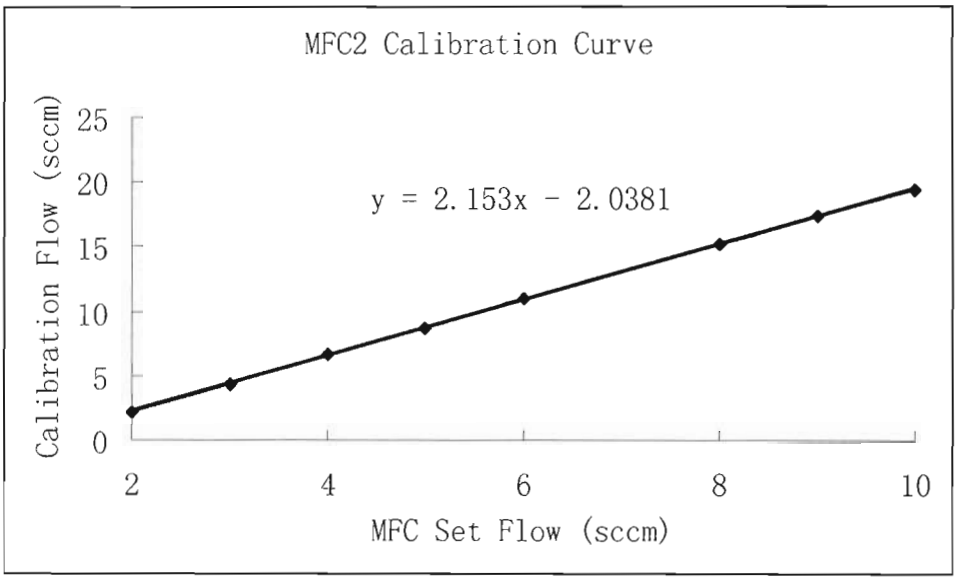

Figure 3.5. MFC2 Calibration Curve.

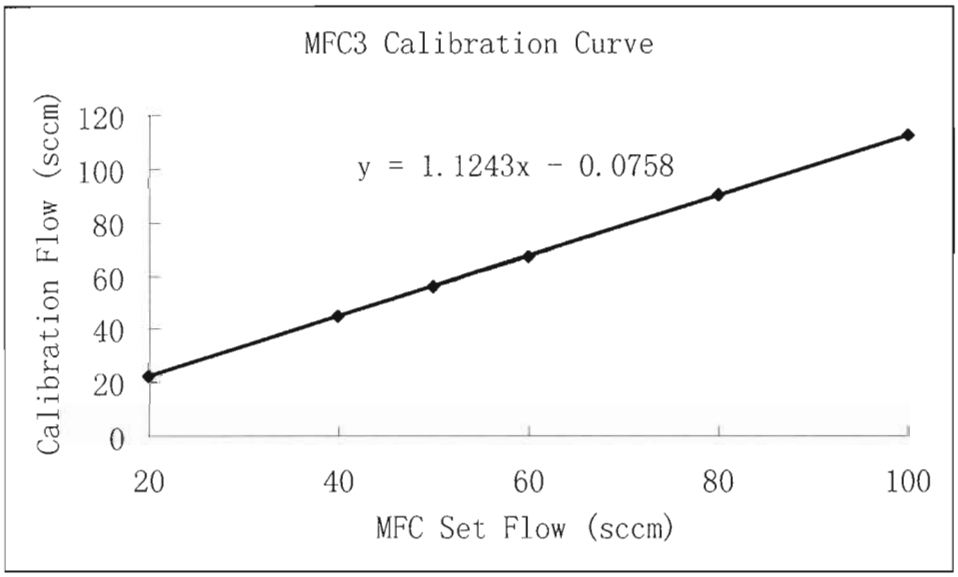

Figure 3.6. MFC3 Calibration Curve.

Table 3.1. MFC calibration values and uncertainties.

MFC's	MFC Calibration equation: y=ax+b			
	a	uncertainty of a	B	uncertainty of b
MFC1	1.0881	0.00541	-1.8147	0.328
MFC2	2.153	0.0105	-2.0381	0.0676
MFC3	1.1243	0.000993	-0.075773	0.0634

3.3. Reactor Response Time for Different Flow Rates

At a suitable sampling time, the target compound should be collected into the sampling loops at steady state. To determine the correct sampling time, we measured the reactor response time at different flow rates. Figure 3.7 shows our initial measurements of the reactor response time, relative to the time when the Y2 valve was switched to the feed mode. At time zero, valve Y2 was changed from vent to feed mode, and the gas stream was sampled in short time intervals until all 16 loops were filled, each sampling time being determined by the GC method and controlled by the data acquisition computer. All of the samples were analyzed with the GC/MS. Figure 3.7 shows that the lower the flow rate, the longer the reactor response time to reach steady state concentration. For example, the response time for a flow rate of 8 sccm is only 5 minutes, but it increases to about 13 minutes for a flow rate of 2 sccm. To decrease the reactor response time, we added a needle valve to the system, as shown in Figure 2.1. Before starting the measurements, the head pressure, P2, was maintained at the same value as the reactor pressure, P3, by adjusting the needle valve. In this way, the response time caused by the pressure differential would be reduced (without the needle valve, P2 is about 0 psig when Y2 is in vent mode). Results showed that the reactor response time for different flow rates was always smaller than 2 minutes after the application of needle valve. Table 3.2 shows the comparison of response time with the flow rate 6 sccm before and after the needle valve was installed.

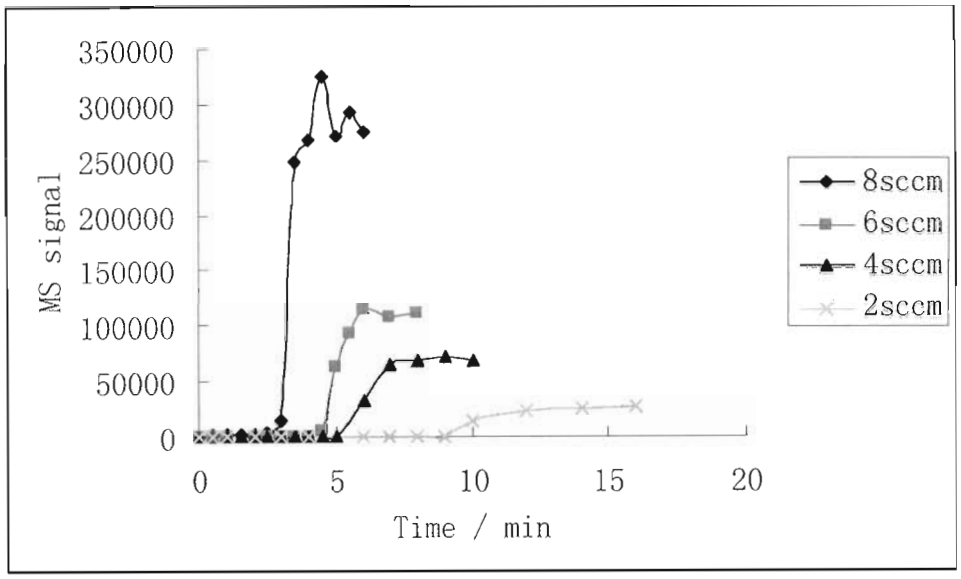

Figure 3.7. Reactor response time for different flow rates when the reactant was turned on before the needle valve Y3 was installed.

Table 3.2. Comparison of response time when the reactant was turned on

Flow rate is 6 sccm	Onset	Stable state
Without needle valve	4.5 min	6 min
With needle valve	0.4 min	1.5 min

Figure 3.8 shows the reactor response time when valve Y2 was switched to vent. When measuring the decay time, the system was already in steady state. At time zero, the valve Y2 was changed to vent mode from the feed mode, and then the same measurements were made as in measuring the "rise" time (see Figure 3.7.). The results showed that the reactor response time does not change with the sample flow rates, and the response time to reach a steady state (MS signal = 0) was always about 3 minutes.

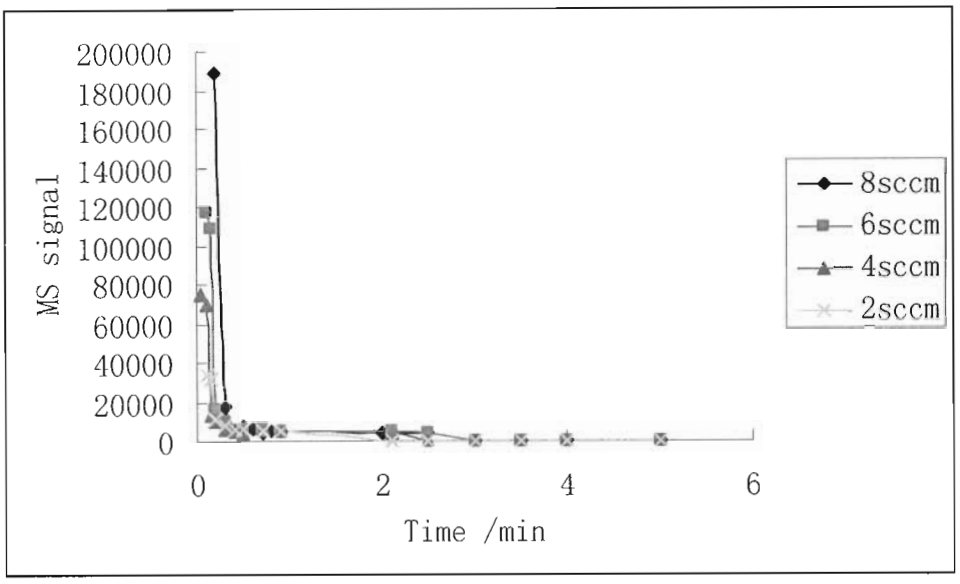

Figure 3.8. Reactor response time for different flow rates when reactant was turned off.

3.4. Pressure Gauge Calibration

Pressure gauges, P1, P2 and P3 were less expensive gauges and have a bigger uncertainty compared to the test gauge P4, which is used to measure the loop pressure. Since P4 is more accurate, it has been taken as a reference to calibrate gauges P1, P2 and P3. The calibration procedure used was as follows: 1) seal the reactor vent to prevent gas from leaking out of the system; 2) set the zero air pressure to a specific value which is in the test gauge pressure range; 3) record the values of each pressure gauge when the pressures are stable; 4) increase the zero air pressure and repeat the procedures. The calibration curves for gauges P1, P2 and P3 are shown in Figure 3.9.

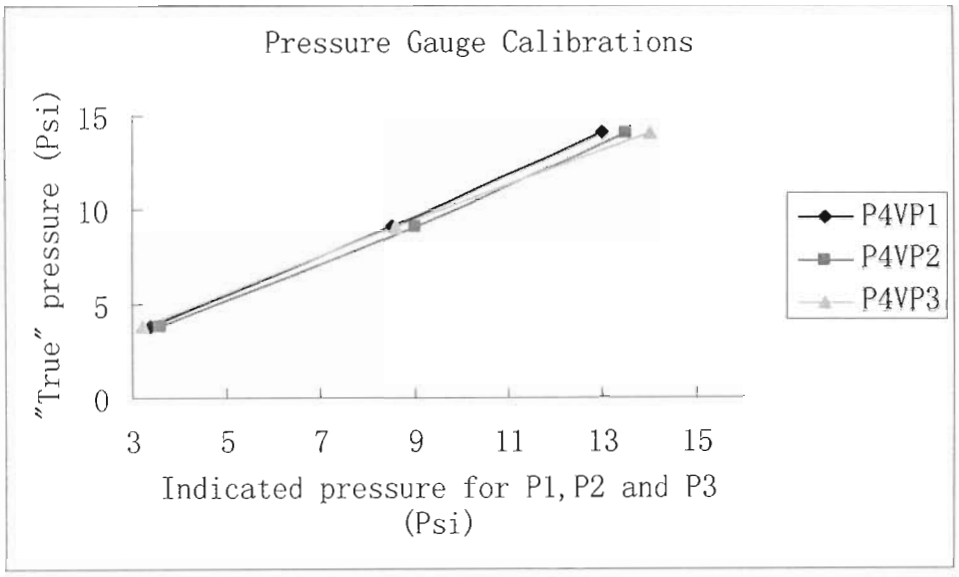

Figure 3.9. Pressure gauge calibration curves.

By making these calibrations, the uncertainties in the gauge pressures are reduced, which will reduce the relative uncertainty in the concentrations in the quantitative analysis procedures (see section 3.8.). The calibration coefficients and their uncertainties are shown in Table 3.3.

Table 3.3. Pressure gauge calibration coefficients and their uncertainties.

Pressure gauge	Pressure gauge calibration equation: y=ax+b			
	a	uncertainty of a	b	uncertainty of b
P4VP1	1.0722	0.0206	0.10098	0.19
P4VP2	1.0385	0.037	-0.034615	0.355
P4VP3	0.9537	0.016	0.79815	0.155

3.5. System Pressure Drop Calculation

Pressure drop is a term used to describe the differential pressure that a fluid must overcome to flow through a system. Since excessive pressure drop will result in poor system performance, the pressure drop must be carefully considered in doing the system design. In this section, the microreactor pressure drop (due to the packed catalyst), tubing pressure drop and valve pressure drop are calculated and presented.

3.5.1. Microreactor Pressure Drop

For gas-phase reactions, the concentration of the reacting species is proportional to the total pressure. In many instances, the effects of pressure drop must be properly accounted to get a successful reactor operation[41].

In this thesis, the pressure drop of the microreactor system was calculated by using the Ergun equation[41, 42]:

$$\frac{dP}{dz} = -\frac{G}{\rho g_c D_p}\left(\frac{1-\phi}{\phi^3}\right)\left[\frac{150(1-\phi)\mu}{D_p} + 1.75G\right] \qquad (1)$$

where P is the pressure; ϕ is the porosity (volume of void/total bed volume); g_c is the conversion factor (for metric system, g_c=1); D is the diameter of particles in the bed; μ is the viscosity of gas passing through the bed; z is the length down the packed bed of pipe; and G is the superficial mass velocity.

The analytic solution of the Ergun equation is expressed as follow (assumptions: isothermal and no change in molar flow rate):

$$\frac{P}{P_0} = \left(1 - \frac{2\beta_0 z}{P_0}\right)^{1/2} \tag{2}$$

$$\beta_0 = \frac{G}{\rho_0 g_c D_p}\left(\frac{1-\phi}{\phi^3}\right)\left[\frac{150(1-\phi)\mu}{D_p} + 1.75G\right] \tag{3}$$

where P_0 is the pressure at the top of the reactor and ρ_0 is the gas density at the top of the reactor bed.

The pressure drop of the microreactor system was carried out in Mathcad, and the source code is attached in **Appendix C**. The Ergun equation shows that the smaller the particle size, the larger the pressure drop (with the same packing length). The pressure drop also increases with increasing microreactor temperature, since the gas viscosity varies with temperature. The relationships of gas viscosity and temperature, pressure drop and temperature, pressure drop and particle size are shown in Figures 3.10 and 3.11 respectively.

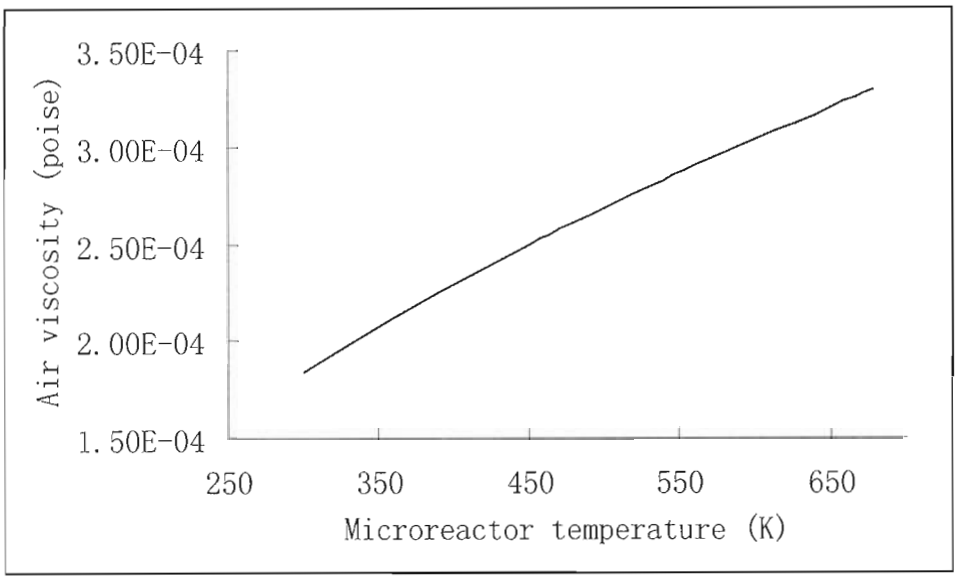

Figure 3.10. Air viscosity varies with temperatures.

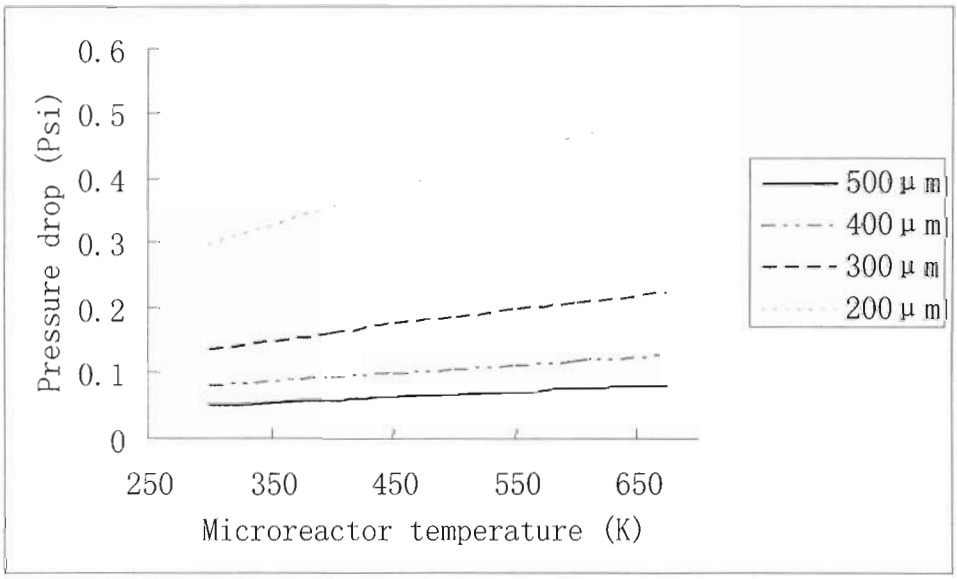

Figure 3.11. Microreactor pressure drop varies with temperatures and particle sizes (All pressure drops were calculated with 25 psi (absolute pressure) entering pressure and 1 inch packing length).

To successfully deliver the gas though the reactor, the pressure drop is expected to be a small value compared to the driving pressure (zero air pressure). That is why the Denstone support media with bigger particle size (see section 2.2.1.) was selected. The calculated pressure drop caused by the packed Denstone support media ranges from 0.442 (at 20°C) to 0.719 psi (at 400°C), and the pressure drop caused by WO_3 ranges from 2.019 (at 20°C) to 3.761 psi (at 400°C). The range of the total reactor pressure drop is from 2.461 to 4.480 psi over the reactor temperature range. All of the pressure drop values were calculated with the Mathcad code in **Appendix C**. All the calculations were made by assuming that all the catalysts had sphere shapes and the porosity of catalysts was 0.4, but the actual porosity was currently not known because of the irregular particle shapes. Our calculations showed that small difference in porosities would result in large changes in the pressure drop, e.g. the pressure drop calculated with 0.36 porosity was about 1.5 times that calculated with 0.4 porosity (see Figure 3.12).

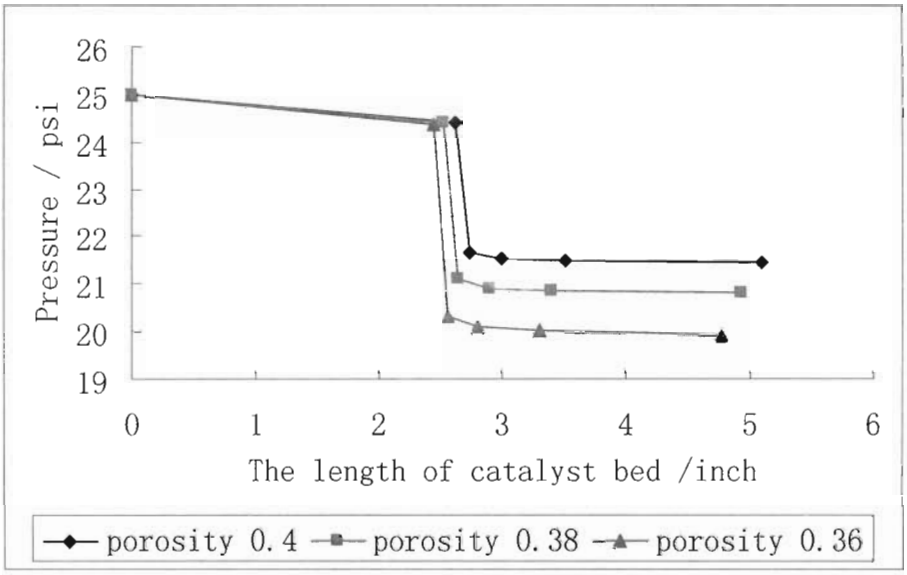

Figure 3.12. Pressure drop profile along the catalyst bed (Denstone support media with 250mg nonporous WO_3).

3.5.2. Tubing and Valves Pressure Drop

The pressure drop in tubing was calculated by using the Poiseulle equation[43]:

$$F=(\pi r^4 \Delta P)/(8\mu L) \qquad (4)$$

where F is the volumetric flow rate; r is the internal radius of the tube; ΔP is the pressure drop between the two ends; μ is the gas viscosity and L is the length of tubing.

The tubing used in the gas delivery system is about 7 feet; the internal radius is 0.0425 inch; the gas flow rate is 250 sccm and the air viscosity is 1.8E-5 $kgm^{-1}s^{-1}$ at room temperature. The calculated pressure drop is 0.044 psi, which can be neglected in comparison with the pressure drop due to the packed bed of the microreactor.

In both the upstream operating mode and downstream operating mode, the gas flow always goes through valve 1 three times and valve 2 twice. Three grooves are located on the valve rotor surface for each six-port, two-position valve. In valve 1 and valve 2, the length of each groove is 0.5 inch, and the port size is 0.030 inch. The calculated pressure drop due to valves is totally 0.083 psi. However, the actual pressure drop caused by valves is seems to be bigger than the calculated value, perhaps because of misalignment between the grooves and the ports of the valve.

3.5.3. Adjustment of Driving Pressure

The pressure at the outlet of the Zero Air Generator is critical because it is the driving pressure which forces the gas to flow through the MFCs and through the bed and valves. The head pressure is the pressure in the head space of the VLE. Because the building's air compressor varies with time, we needed to increase the head pressure until the MFC flow rate was independent of the pressure. To make a successful gas delivery, the head pressure should be bigger than the pressure drop of the system. Considering the effect of temperature, tube bending, glass wool (packed in the reactor to support Denstone media and WO_3 powder) and connectors, we estimated the total pressure drop of the system was about 7 psi. The zero air pressure must be bigger than the head pressure to drive the gas passing through the MFCs, and the pressure difference is proportional to the gas flow rate. To determine the acceptable zero air pressure, we measured the reference pressure P4 with different zero air pressure (see Figure 3.13.)

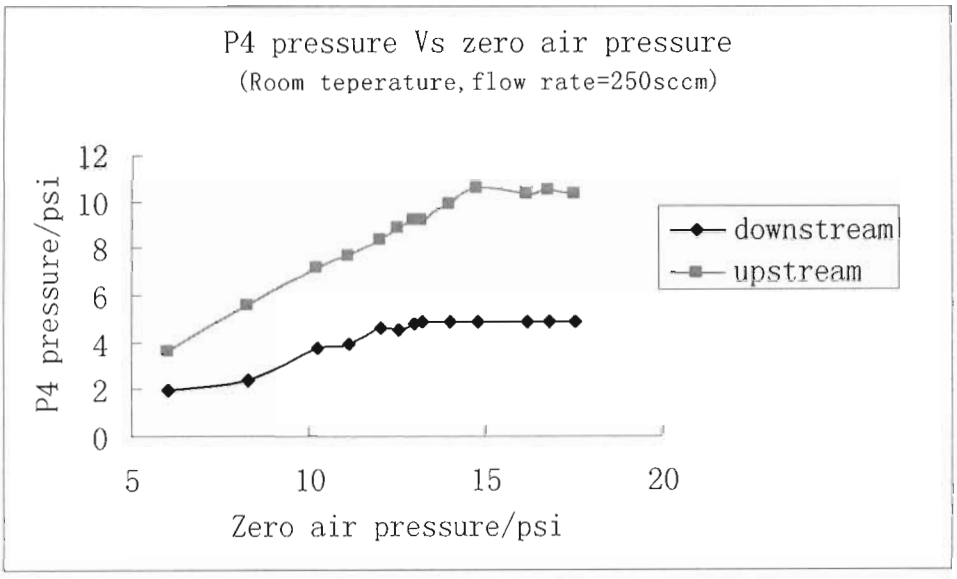

Figure3.13. The relationship of P4 and driving pressure at room temperature.

Figure 3.13 shows that P4 is a constant when the driving pressure is more than 15 psi for both downstream and upstream operating modes, which means that the system is in steady state. Compared to room temperature, the system pressure drop is increased by 2 psi at 400°C. Consequently, the driving pressure must be more than 17 psig to get a steady state. During our experiments, driving pressure was set to 24 psig.

3.6. GC Operating Conditions

3.6.1 Sampling Time

In our experiments, the first 8 loops of valve 3 were sampled in upstream mode; the other 8 loops were sampled in downstream mode. To ensure that the loops will be filled at the steady state concentration, the sampling time should be carefully determined.

Considering the reactor response time measurements in section 3.3, the response time for a flow rate of 8 sccm should be no smaller than 5 minutes. However, valve 1 was in downstream mode and valve 2 was in "inject" mode initially. When the sampling started, valve 1 was changed to upstream mode and valve 2 changed to sampling mode respectively. These changes induced a pressure balancing time (due to the change of gas pathway) of about 4 minutes. Hence the time to feed the first loop should no smaller than 9 minutes. We set the first sampling time to be 16 minutes, and the upstream and

Table 3.4. Sampling method for uptream and downstream operating mode.

Time/min	Item	Setting mode
0	Valve 1	On (upstream)
0	Valve 2	On (sampling)
16	Valve 3	Inject
17	Valve 3	Inject
18	Valve 3	Inject
19	Valve 3	Inject
20	Valve 3	Inject
21	Valve 3	Inject
22	Valve 3	Inject
23	Valve 3	Inject
23	Valve 1	Off (downstream)
23	Valve 2	On (sampling)
39	Valve 3	Inject
40	Valve 3	Inject
41	Valve 3	Inject
42	Valve 3	Inject
43	Valve 3	Inject
45	Valve 3	Inject
46	Valve 3	Inject
47	Valve 3	Inject

downstream sampling method is shown in Table 3.4. The "inject" for valve 3 listed in Table 3.4 means valve 3 is rotated, capturing a sample of the target compound in the sampling loop. After sampling is complete, valve 2 is set to "inject" and the sample in the first loop is delivered into the GC/MS with the carrier gas. For subsequent loops, valve 3 is rotated, injecting the gas sample into the GC/MS. Right after upstream sampling, the downstream sampling is performed, with the same sampling method as upstream except that valve 1 was set to downstream mode.

3.6.2. Oven Temperature

The initial oven temperature should ideally be above the boiling point of the solvent but below the boiling point of the analytes. A lower temperature will retain the compounds on the column longer. Longer retention times may help resolve closely eluting peaks. A slower temperature ramp will separate compounds with similar boiling points with the trade-off of a longer analysis time. The final temperature should be close to or above the boiling point of the least volatile compound in the sample to ensure that none of the sample will remain on the column to contaminate subsequent analyses. The hold time is the length of time the GC oven will be maintained at the final temperature.

For the experiments of methanol on WO_3, three temperature programs were tried (see Table 3.5.). The chromatographs of program 1 and 2 are shown in figure 3.13.

Table 3.5. Parameters of oven temperature programs.

Temp Program	Initial Temp (°C)	Hold time (min)	Ramp Rate (°C/min)	Final Temp (°C)	Hold Time (min)	Total Time (min)
1	60	4.0	X	X	X	4.0
2	-5	3.5	50	50	1.0	5.6
3	-15	3.5	50	50	2.0	6.8

In Figure 3.14a, the small peak with retention time 2.6 min is the methanol peak, which overlaps with the tail of the air peak (RT=2.28); in Figure 3.14b, a well separated methanol peak with retention time 3.79 is observed. Comparing these two oven temperature programs, the initial temperature of -5 °C is more suitable for the quantitative analysis. Because we planned to study not only methanol but also the possible oxidation products, such as formaldehyde and dimethyl ether, whose retention times are very close to methanol, the lower initial temperature of -15°C was employed to separate those compounds.

We planned to study the oxidation of methanol, ethanol, iso-propanol, 2-butanol and 2-hexanol on non-porous and porous WO_3 powders. Due to the different boiling point and retention time of these alcohols, the oven temperature programs were adjusted, and the detailed parameters are shown in Table 3.6.

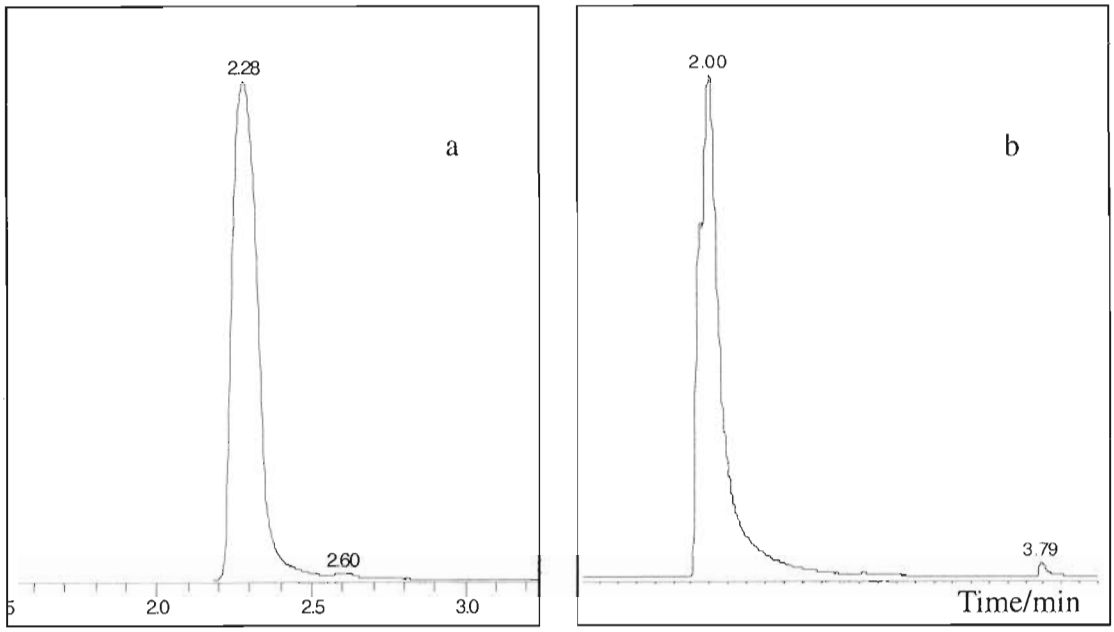

Figure 3.14. Gas chromatographs of methanol with a): Temp program 1 (Initial Temp: 60°C) and b): Temp program 2 (Initial Temp: -5°C).

Table 3.6. Detailed oven temperature program parameters for the series of alcohols.

Sample	Methanol	Ethanol	Iso-propanol	2-butanol	2-hexanol
Initial Temp (°C)	-15	-15	-5	-15	100
Hold Time (min)	3.5	3.5	3.5	3.5	3.5
Ramp Rate(°C/min)	50	50	50	50	50
Final Temp (°C)	50	50	50	100	150
Hold Time (min)	2	3	4	4	6.5
Total Time (min)	6.8	7.8	8.8	9.8	11

3.6.3. Helium Flow Rate

Helium was used as the carrier gas in our experiments. The carrier gas carries the analyte mixture through the GC column, where the mixture is separated into its individual components. The helium flow rate is a significant parameter because it directly influences the retention time and column efficiency. It is necessary to set the proper carrier gas flow rate to get the best analysis time, column efficiency and reproducibility.

The optimum flow rate will depend on the nature of the carrier gas, column diameter, column length, film thickness and other variables. The average linear velocity is easily calculated by using the equation:

$$u = \frac{L}{t_n} \qquad (5)$$

where u is the average linear velocity of carrier gas; L is the column length; and t_n is the retention time of a non-retained solute

The effect of carrier gas average linear velocity on efficiency is best illustrated using a van Deemter curve[44, 45] (see Figure 3.15.), where the lower the H (height equivalent of a theoretical plate) the better the column efficiency. The optimum ranges for He gas velocities are shown in the van Deemter curve, which is between 22 and 35 cm/sec.

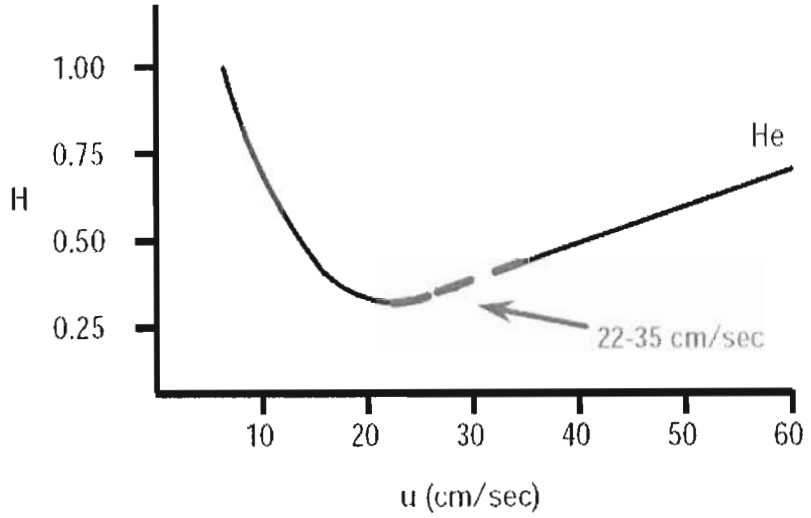

Figure 3.15. Van deemter curve for helium[46].

In our experiments, the helium flow rate was initially set to 2 sccm/min. The gas chromatographs shown in Figure 3.14 used this flow rate. Because air was the non-retained solute in the GC/MS experiments, we could easily get the value of t_n (2.0 to 2.28 min). The length of the DB-1 column we used was about 30 m. The average linear velocity calculated ranged from 22 to 25 cm/sec. By checking the velocity in van Deemter curve, we confirmed that the He flow rate of 2 sccm/min was applicable to get high column efficiency.

3.6.4. Split Ratio

Split ratio is the ratio of split vent flow to the column flow, which determines the amount of the sample entering the column (a higher ratio means that less sample is injected into the column). A very high split ratio will bring the problems of poor

sensitivity and carrier gas waste; a very low split ratio will cause poor peak shape and overloading of the column. For capillary columns, the split ratio is typically 20:1 to 100:1. In our experiments, a split ratio of 30:1 was used.

3.7. MS Operating Conditions

3.7.1. Emission Current

According to the theoretical calculations, the amounts of target compounds in the sampling loop are 10^{-7} to 10^{-8} mole. To get good MS signals of these tiny amounts of compounds, the MS operating conditions need to be optimized.

The filament in the MS ion source is heated by an adjustable ac current. The filament current heats the filament, causing it to emit electrons, and these electrons ionize the sample molecules. By changing the emission currents and monitoring the relative intensity of peak 28 (Carrier gas He, intensity 100), the relation of emission current and MS intensity was illustrated in Figure 3.16.

Figure 3.15 shows that there is a flat intensity plateau when emission current is bigger than 300μA. In the plateau range, the fluctuation of emission current will not affect the MS intensity, which means the MS sensitivity is a constant. Considering that higher emission current will reduce filament life, the current range between 300 and 350μA is preferred.

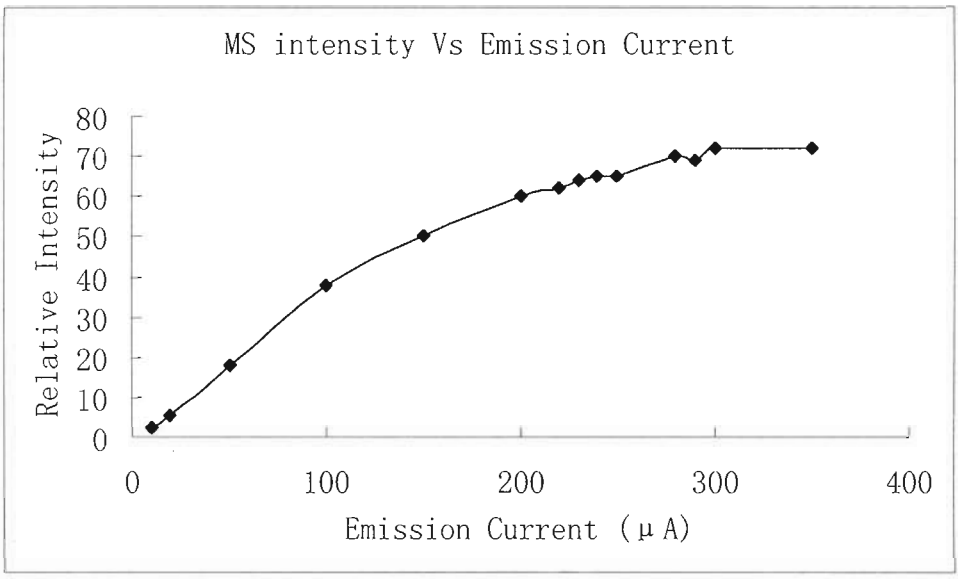

Figure 3.16. The change of MS intensity with increasing emission current.

3.7.2. Detector Voltage

The detector in the mass spectrometer converts the ions that pass through the mass analyzer into an analog current, which is then measured by a picoammeter. When ions leave the ion source they are received into the mass analyzer. The function of the analyzer is to separate the ions and measure their masses. In fact, what is actually measured is the mass to charge ratio (m/z) for each ion. However, since in most cases with electron impact ionization, the charge is unity, the m/z value can be taken as being equivalent to ion mass.

Once the ion passes through the mass analyzer it is then detected and counted by the ion detector. The detector allows a mass spectrometer to generate a signal current from incident ions by generating secondary electrons, which are further amplified. Increasing

the detector voltage will increase the abundances of the ions reported in the scan. Figure 3.17 shows the relation between detector voltage and MS sensitivity. In our experiments, the default MS detector voltage, 350 V was applied.

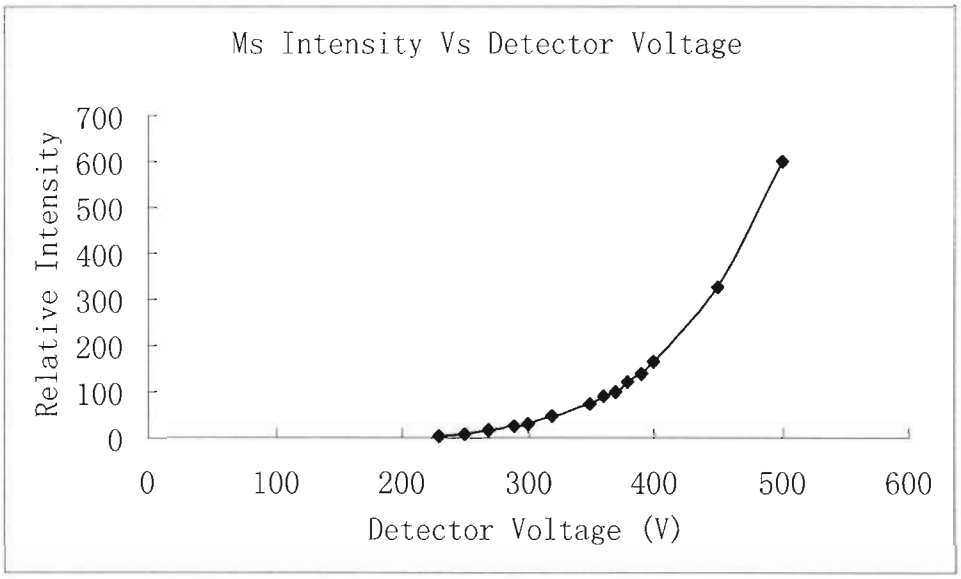

Figure 3.17. The changed of MS intensity with increasing detector voltage.

3.7.3. Tuning

Tuning is the process of adjusting certain parameters to optimize the performance of the instrument. The tune parameters are instrument parameters whose values can vary with the type of experiment. Therefore, TRACE-MS needs to be tuned when the experiment type is changed. Reference material heptacosa (*Fluorochem Limited, 008740*) was used for tuning purposes.

A manual tuning process was performed. The masses of 69 (Intensity, 100%), 264

(8-12%), 502 (1-3%) and 614 (>0.2%) were used for tuning on heptacosa in EI mode. All the tuning parameters were adjusted to optimize the intensity of heptacosa across the full mass range. At the end of the tuning process, the optimized tuning parameters were saved as a *tun* file with a file name *lowgas* (see Table 3.7)

Table 3.7. Tune setting parameters of lowgas.tun method.

Tune Settings Ionization mode: EI+		
Setting	Set Point	Readback
Emission Current (μA):	320	324
Source Current (μA):	n/a	2082.1
Source to Trap Ratio:	n/a	6
Filament Current (A):	n/a	4.0
Repeller Voltage (V):	0.5	0.6
Electron Energy (eV):	70	70.32
Lens 1 (V):	4	6
Lens 2 (V):	30	30
Ion Energy (eV):	1.9	n/a
Ion Energy Ramp (mV/amu):	1.2	n/a
Interface Temperature (°C):	250	255
Source Temperature (°C):	200	80
Low Mass Resolution:	10.5	n/a
High Mass Resolution:	12.6	n/a
Detector Voltage (V):	350	350.7

3.7.4. Spectrum Acquisition

Full scan mode was used for spectrum acquisition. The acquisition rate was 10 scans per GC peak. The mass spectrum was set to scan from 13 to 120 amu. Because the air

peak was too big compared to the target compound (as shown in Figure 3.14) and useless in the quantitative and qualitative analysis, to protect the filament, MS was set to start acquiring spectra at 2.8 minutes after the solvent eluting. The time delay setting for spectrum acquisition was used in all of the alcohol oxidation experiments.

3.7.5. Peak Integration Method

The GC/MS software Xcalibur™ was employed in our experiments. Xcalibur™ is capable of quantitative analysis by using either peak area or peak height and employs mathematical algorithms related to the slope of the response to detect the beginning and end of peaks. This data system allows automatic peak area integration with adjustable instrument parameters. However, regardless of the sophistication of this software, instances occur when the automated software does not integrate a peak correctly. The failure of the software to appropriately integrate a peak is usually obvious from visual inspection of the chromatogram (see Figure 3.18.). Figure 3.18a shows the automatic integrated area (AA) and Figure 3.18b shows the manual integrated area (MA). It is apparent that the automatic integrated area is smaller than the manual integrated area.

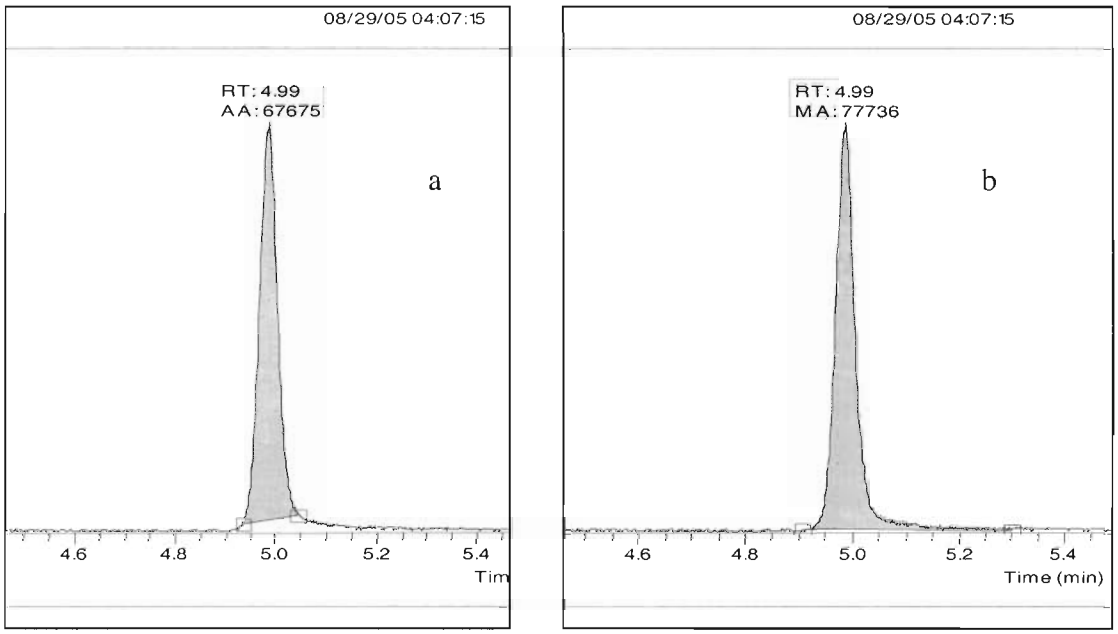

Figure 3.18. Integration method:a) Automatic integration; b) manual integration.

Manual integration was necessary to provide accurate quantitation of peak areas, because the automatic peak limits chosen for integration by the data system roughly doubled the experimental uncertainty in a replicate set. Additionally, in some cases the data system might misidentify the peak; this situation must be corrected by manual integration. To carry out a manual integration one must consider the chromatographic baseline and the start and stop points of the peak along the baseline. When manual integration is used, it is helpful to zoom in on the baseline (see Figure 3.19.). Instrument peaks must be consistently integrated and reported according to proper techniques, generally baseline-to-baseline, valley-to-valley, or a combination of the two. Improper peak integration, artificially reducing (Figure 3.19b) or enhancing (Figure 3.19c) peak area, will produce an erroneous area. In our experiments, the average noise level of the

baseline was determined. The start and stop points for each peak were carefully set at the average noise level of the baseline (see Figure 3.19a).

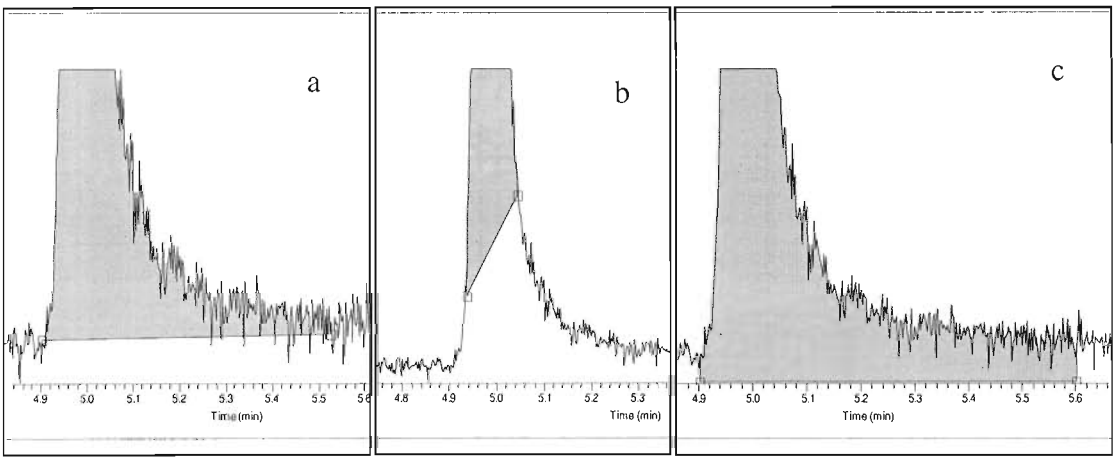

Figure 3.19. MS peak integration. a): Proper integration; b): Peak shaving; c): Peak enhancing.

3.8. Quantitative Analysis

To have a through understanding of the reproducibility of the experiment, we have calculated the concentrations and the uncertainties in the concentrations for the calibration gas which goes to the GC in the upstream operating mode.

In the methanol (in VLE) concentration calculations, we calculated the uncertainty caused by temperatures, flow rates, loop volumes and gauge pressures. The detailed calculation procedures are shown in **Appendix A**.

The mole fraction of methanol in the VLE was calculated by the equation:

$$X = \frac{P_{Meth}}{(P_{atm} + P_{gauge})} \tag{6}$$

where X is the mole fraction of methanol in the VLE; P_{Meth} is the partial pressure of methanol; P_{atm} is the atmosphere pressure and P_{gauge} is the gauge pressure. The uncertainty of the methanol mole fraction in the VLE was calculated by the equation:

$$(\partial X)^2 = \frac{1}{(14.7 + P_{gauge})^2} \cdot (\partial P_{Meth})^2 + \frac{P_{Meth}^{\ 2}}{(14.7 + P_{gauge})^4} \cdot (\partial P_{gauge})^2 \tag{7}$$

The partial pressure of methanol at different temperatures was calculated by using the Antoine Equation:

$$LogP_{meth} = A - \frac{B}{T + C} \tag{8}$$

where A, B and C are the Antoine constants; T is the temperature with unit °C; $P_{Meth}$is the partial pressure of methanol with unit torr. From this equation, we can also get the uncertainty of the methanol partial pressure caused by the Antoine constants and temperature.

The uncertainty in the number of moles of reactant in the sampling loop, from which the mass spectra sensitivity is determined, depends on the particular set of operating parameters. As an example, in Table 3.8, we list the uncertainties of the most significant factors and their contributions to the relative uncertainty of methanol concentration in the sampling loop. In the uncertainty calculation, the most significant parameter is the

Table 3.8. Relative uncertainties of methanol concentration in sampling loop due to system uncertainties (The calculated amount of MeOH in loop (n_P) is 9.6705×10^{-8} mole using values from Appendix A, F_{1c}, F_{2c} and F_{3c} are calibrated flow rates).

Parameter (P)	Uncertainty (σ)	Mole of MeOH in loop/mole ($n_{P+\sigma}$)	Mole of MeOH in loop/mole ($n_{P-\sigma}$)	Slope $(n_{P+\sigma}-n_P)/\sigma$	$(\delta n_P)^2$	Relative uncertainty in n_P
T_{VLE}=20°C	2.2°C	1.097E-7	8.512E-8	5.586E-9	1.51E-16	12.7%
P1=12psig	0.35psi	9.6707E-8	9.6702E-8	7.12E-12	6.25E-24	0.0003%
P2=12.5psig	0.60psi	9.4415E-8	9.9109E-8	-3.89E-9	5.51E-18	3.2%
P4=5.28psig	0.035psi	9.6874E-8	9.6536E-8	4.829E-9	2.86E-20	0.175%
F_{1c}=41.71sccm	0.67sccm	9.6468E-8	9.6943E-8	-3.85E-10	6.68E-20	0.267%
F_{2c}=8.73sccm	0.23sccm	9.4222E-8	9.9183E-8	1.071E-8	6.15E-18	2.56%
F_{3c}=224.78sccm	0.60sccm	9.6496E-8	9.6915E-8	-3.49E-10	4.38E-20	0.21%
T_{loop}=21°C	2.2°C	9.5987E-8	9.7434E-8	-3.29E-10	5.23E-19	0.748%
V_{loop}=0.75cm^3	0.02 cm^3	9.9284E-8	9.4126E-8	1.29E-7	6.65E-18	2.667%

uncertainty of the VLE temperature, which generates 12.7% relative uncertainty in the concentration. The other three significant contributions to the relative uncertainty are the uncertainties of pressure P2, flow rate F_{2c}, and the loop volume V_{loop}. While the total uncertainty in the absolute concentration is 22.5%, the reproducibility of the spectra was much better. The reproducibility of the sampling loop volume should be negligibly small, and the reproducibility of the thermocouple measurement (measured to 0.5°C) should allow the T_{VLE} contribution to be reduced to 2.9%.

The reproducibility of the system was tested before we started the experiments and can be compared to error analysis of the previous paragraph. At room temperature, MFC1, 2 and 3 were set 40, 5 and 200 sccm respectively, and the gas stream (methanol, water vapor and synthetic air) was collected in all 16 loops under the same condition and then analyzed with the GC/MS. By comparing the methanol peak area in the GC/MS spectrum, the difference in loop volumes could be estimated. Figure 3.20 shows the methanol peak area for each sampling loop. The relative uncertainty of the peak area was 3.6% for upstream experiments and 5.3% for downstream experiments. Both of the uncertainties are much smaller than the calculated total uncertainty, 22.5%, which means the reproducibility of the sampling loop volume could be negligible.

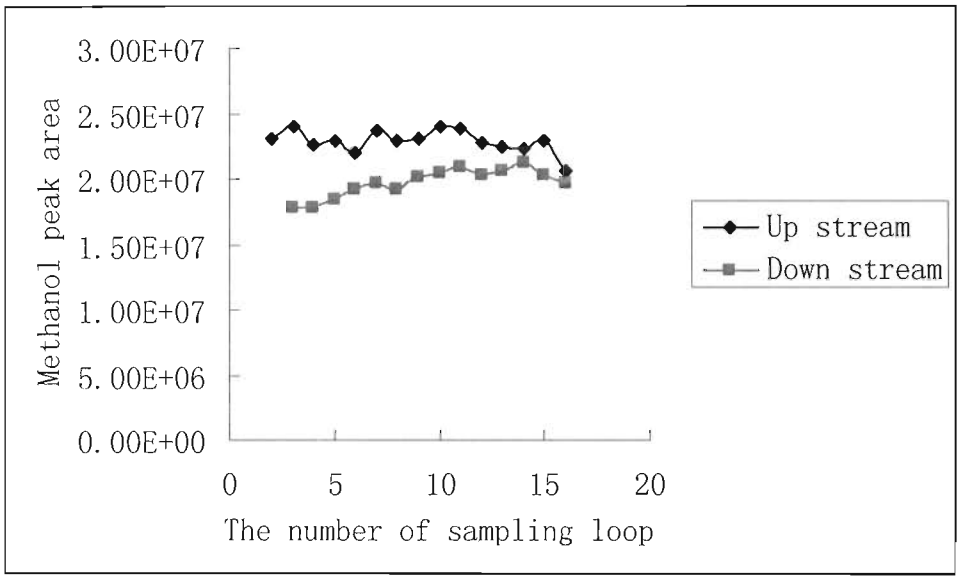

Figure 3.20. Integrated methanol peak area of each sampling loop.

Chapter 4

RESULTS AND DISCCUSSION

4.1 Introduction

Technologically, most valuable chemicals obtained by alcohol oxidation reactions are hydrocarbons containing oxygen containing functional groups, such as aldehydes, ethers, and ketones, which are intermediates on the way to the total oxidation, thermodynamically stable products CO_2 and H_2O. Therefore, the selectivity of their formation strongly depends on the conditions of the reaction, e.g. temperature, contact time, diffusional parameters, efficiency of heat transport, flow rate, etc[47]. The selectivity of alcohol oxidation reactions also depends on the properties of the catalyst. Ai[48] has related the catalytic activity of various mixed oxides for selective oxidation of methanol to the acid-base character the active sites of the oxides. Wachs and coworkers[26, 27, 49] also reported that selective oxidation of methanol and 2-propanol was strongly associated with the acidity and basicity of metal oxides.

In this chapter, selective oxidation product distributions of alcohols on different catalysts, Al_2O_3, nonporous WO_3/Al_2O_3, and porous WO_3/Al_2O_3, are presented in detail. The reaction conditions for all of the alcohols were similar. Therefore, the activities of these catalysts for selective oxidation of alcohols could be compared by analyzing the product distributions. Because we are interested in the oxidation of alcohols under conditions relevant to sensor operations, we chose 15% relative humidity in the reactant stream, which is significantly higher than in the conditions that have been reported in the

catalysis literature. The water vapor in the overall stream probably accounts for the strong effects on the alcohol oxidation reactions in comparison to the literature. Since "blank" experiments (pure Denstone support media as the catalyst bed) showed large activity toward alcohol oxidation, alcohol conversion as a function of temperature for Al_2O_3, nonporous WO_3/Al_2O_3, and porous WO_3/Al_2O_3 showed that only 2-butanol oxidation at 100 and 200°C was dominated by the activity of WO_3. To study the activity of nonporous and porous WO_3, kinetic analysis of 2-butanol on these catalysts were also presented and compared.

4.2. Alcohol Oxidation Product Distribution

Alcohol oxidation products were identified by referring to the spectral library in the Xcalibur program and the NIST (National Institute of Standards and Technology) online MS spectral database. The online gas chromatography database (NIST Chemistry WebBook) was also employed for the identification of the alcohol oxidation products. During our experiments, the same product distribution was observed on nonporous WO_3/Al_2O_3 and porous WO_3/Al_2O_3, so no distinction will be made in the Tables in this section between them.

4.2.1. Methanol on Al_2O_3 and WO_3/Al_2O_3

No oxidation product was detected when methanol passed through the pure Denstone support media in the reactor temperature range between room temperature and

400°C. However, any CO and CO_2 produced would not be separated chromatographically from the air peak.

At 250°C, 300°C, 350°C and 400°C, dimethyl ether was observed as the sole oxidation product of methanol on WO_3/Al_2O_3; at or below 200°C, no products were detected (See Table 4.1).

Table 4.1. Methanol oxidation product distribution on Al_2O_3 and WO_3/Al_2O_3.

Temperature (°C)	≤200	250	300	350	400
Oxidation product on Al_2O_3	None	None	None	None	None
Oxidation product on WO_3/Al_2O_3	None	Dimethyl ether	Dimethyl ether	Dimethyl ether	Dimethyl ether

4.2.2. Ethanol on Al_2O_3 and WO_3/Al_2O_3

Below 200°C, no ethanol oxidation products were detected on both Al_2O_3 and WO_3/Al_2O_3. At higher temperature, the oxidation products of ethanol varied with increasing temperature, and the product distribution is shown in Table 4.2.

Table 4.2. Ethanol oxidation product distribution on Al_2O_3 and WO_3/Al_2O_3.

Temperature (°C)	≤200	250	300	350	400
Oxidation products on Al_2O_3	None	None	Acetaldehyde	Acetaldehyde Acrolein	None
Oxidation products on WO_3/Al_2O_3	None	Ethyl ether	Ethyl ether Acetaldehyde	Ethyl ether Acetaldehyde Acrolein	Acetaldehyde Acrolein

4.2.3. 2-propanol on Al_2O_3 and WO_3/Al_2O_3

The 2-propanol oxidation product distributions on Al_2O_3 and WO_3/Al_2O_3 were the same: at low temperature, no products were detected; at 250°C, acetone was the sole product; at higher temperatures, both acetone and methyl vinyl ketone were detected.

Table 4.3. 2-propanol oxidation product distribution on Al_2O_3 and WO_3/Al_2O_3.

Temperature (°C)	≤200	250	300	350	400
Oxidation products on Al_2O_3	None	Acetone	Acetone Methyl vinyl-ketone	Acetone Methyl vinyl-ketone	Acetone Methyl vinyl-ketone
Oxidation products on WO_3/Al_2O_3	None	Acetone	Acetone Methyl vinyl-ketone	Acetone Methyl vinyl-ketone	Acetone Methyl vinyl-ketone

4.2.4. 2-butanol on Al_2O_3 and WO_3/Al_2O_3

When the reactor temperature was below 200°C, no oxidation products were detected on Al_2O_3. At higher temperatures, the oxidation products were almost the same, except for the appearance of isopropenyl methyl ketone at 300 and 350°C.

At room temperature, no product was detected when 2-butanol passed through the WO_3/Al_2O_3 catalyst. Between 100 and 350°C, several products were always detectable (see Table 4.4.), and 2-butanone only appeared in the products at 250, 300 and 350°C. Isopropenyl methyl ketone was also detected at 300 and 350°C over the WO_3/Al_2O_3 catalyst.

Table 4.4. 2-butanol oxidation product distribution on Al_2O_3 and WO_3/Al_2O_3

Temp (°C)	100	200	250	300	350
Oxidation products on Al_2O_3	None	None	1-butene trans-2-butene cis-2-butene 2-butanone	1-butene trans-2-butene cis-2-butene 2-butanone Isopropenyl-methyl ketone	1-butene trans-2-butene cis-2-butene 2-butanone Isopropenyl-methyl ketone
Oxidation products on WO_3/Al_2O_3	1-butene trans-2-butene cis-2-butene	1-butene trans-2-butene cis-2-butene	1-butene trans-2-butene cis-2-butene 2-butanone	1-butene trans-2-butene cis-2-butene 2-butanone Isopropenyl-methyl ketone	1-butene trans-2-butene cis-2-butene 2-butanone Isopropenyl-methyl ketone

4.2.5. 2-hexanol on Al_2O_3 and WO_3/Al_2O_3

2-hexanone was the only product detected at 200, 250, and 300°C during the experiments of 2-hexanol oxidation on Al_2O_3. But no products were detected at both low temperature (100°C) and high temperature (350°C).

Between 200 and 350°C, the oxidation products of 2-hexanol on WO_3/Al_2O_3 were the same (see Table 4.5.), including 1-hexene, trans-2-hexene, cis-2-hexene and 2-hexanone. However, at 100°C, only trans- and cis-2-hexene were detectable.

Table 4.5. 2-hexanol oxidation product distribution on Al_2O_3 and WO_3/Al_2O_3

Temp (°C)	100	200	250	300	350
Oxidation products on Al_2O_3	None	2-hexanone	2-hexanone	2-hexanone	None
Oxidation products on WO_3/Al_2O_3	trans-2-hexene cis-2-hexene	1-hexene trans-2-hexene cis-2-hexene 2-hexanone	1-hexene trans-2-hexene cis-2-hexene 2-hexanone	1-hexene trans-2-hexene cis-2-hexene 2-hexanone	1-hexene trans-2-hexene cis-2-hexene 2-hexanone

4.3. Alcohol Conversion

The detailed experimental conditions have been shown in Tables 2.1 and 2.2 (see Chapter 2), including the information of MFC flow rates and catalyst weights. The alcohol conversion was calculated by the equation:

$$\text{Conversion} = [C-(A/\alpha)]/C \qquad (1)$$

where A is the MS peak area for the down stream mode; α is the MS sensitivity determined from the up stream mode; C is the initial alcohol concentration calculated for the down stream mode conditions; and A/α is the actual alcohol concentration in the sampling loop in the down stream mode. The MS peak areas were determined by manual integration of the mass spectrum. Calculations of the MS sensitivity and alcohol concentration are shown explicitly in the Mathcad code listed in Appendix A. Since the MS sensitivity and concentration did not change too much, the uncertainty of the conversion was proportional to the peak area. Therefore, the conversion uncertainty was big (large error bar) at low temperature (low conversion) and small (short error bar) at high temperature (high conversion) for each conversion curve. Because the uncertainty of the actual alcohol concentration (A/α) is always bigger than the uncertainty of the initial concentration (C), negative conversion can result from the calculations (see equation (1)) when the actual conversion is small.

From 250 to 400°C, methanol dehydration to dimethyl ether occurred on both nonporous and porous WO_3/Al_2O_3. Although no product was detected in the experiments of methanol on Al_2O_3, methanol was consumed at higher temperatures, which can only

be attributed to complete oxidation products (CO, CO_2 and H_2O). Figure 4.1 shows the observed methanol conversion as a function of temperature for the three types of catalysts. For each catalyst the conversion increases as the reaction temperature increases.

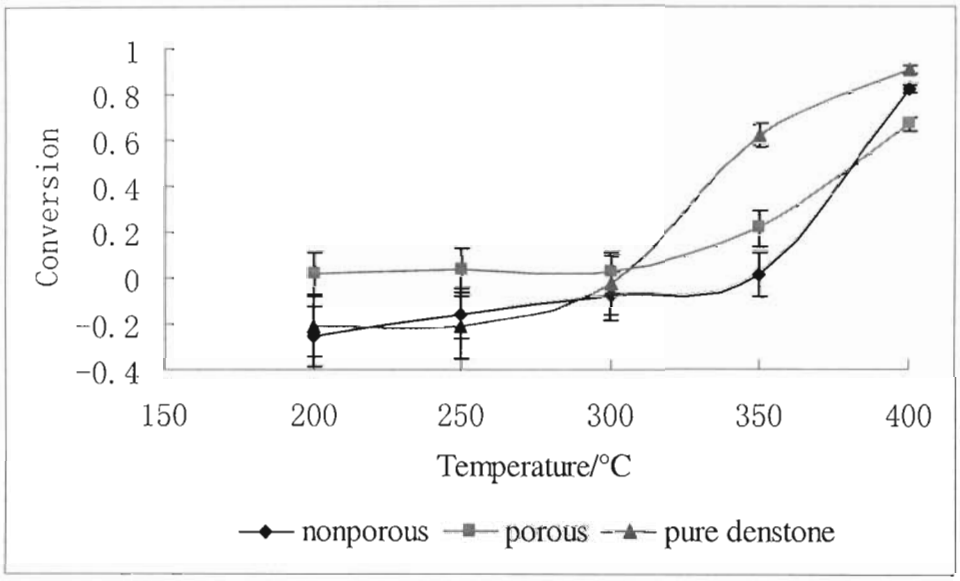

Figure 4.1. Comparison of methanol conversion versus reaction temperature on nonporous WO_3/Al_2O_3, porous WO_3/Al_2O_3, and Al_2O_3 (pure Denstone support).

The following four figures show the conversion for the other alcohols at different reaction temperatures on nonporous WO_3/Al_2O_3, porous WO_3/Al_2O_3, and Al_2O_3. In each figure, the alcohol conversion increases as the reaction temperature increases for all of the catalysts. For each alcohol oxidation on the three catalysts, the reaction conditions were different, e.g. the MFC1 flow rates were changed according to the catalysts (see

Table 2.2); the weights of nonporous and porous WO_3 powders were different (see Table 2.1); and the pressure of P2 and P4 were different due to the pressure drop. All of these differences in reaction conditions mean that the alcohol conversion on these three catalysts can not be compared directly.

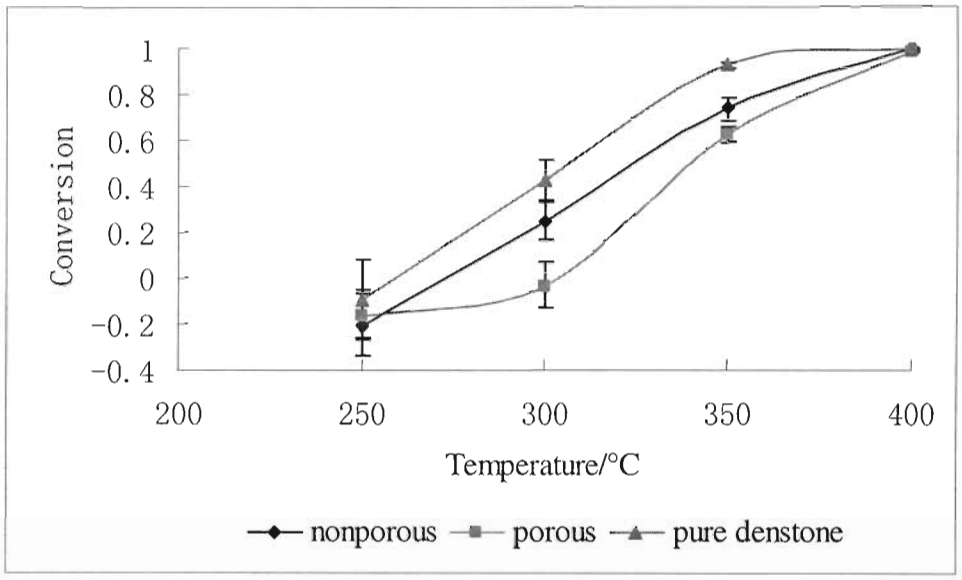

Figure 4.2. Comparison of ethanol conversion versus reaction temperature on nonporous WO_3/Al_2O_3, porous WO_3/Al_2O_3, and Al_2O_3 (pure Denstone support).

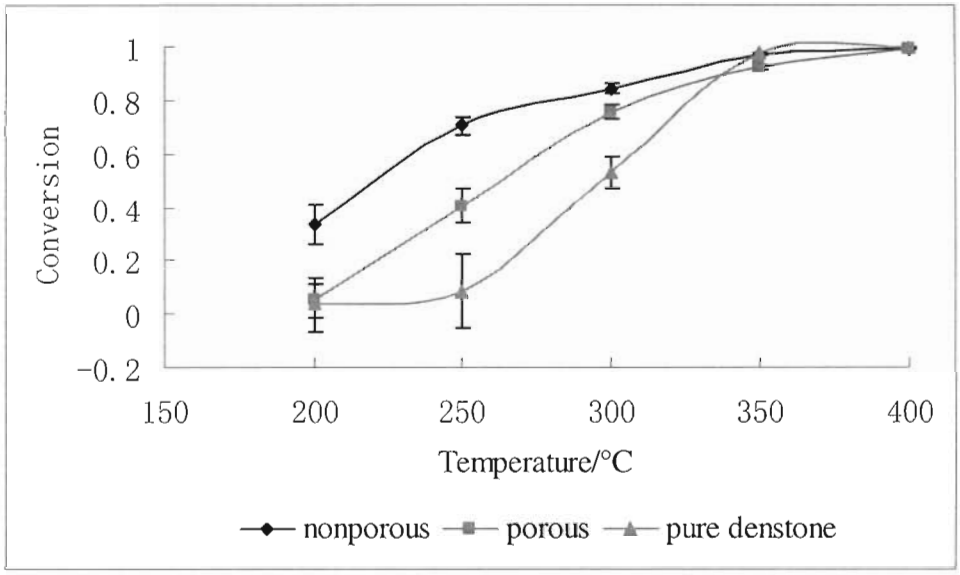

Figure 4.3. Comparison of 2-propanol conversion versus reaction temperature on nonporous WO_3/Al_2O_3, porous WO_3/Al_2O_3, and Al_2O_3 (pure Denstone support).

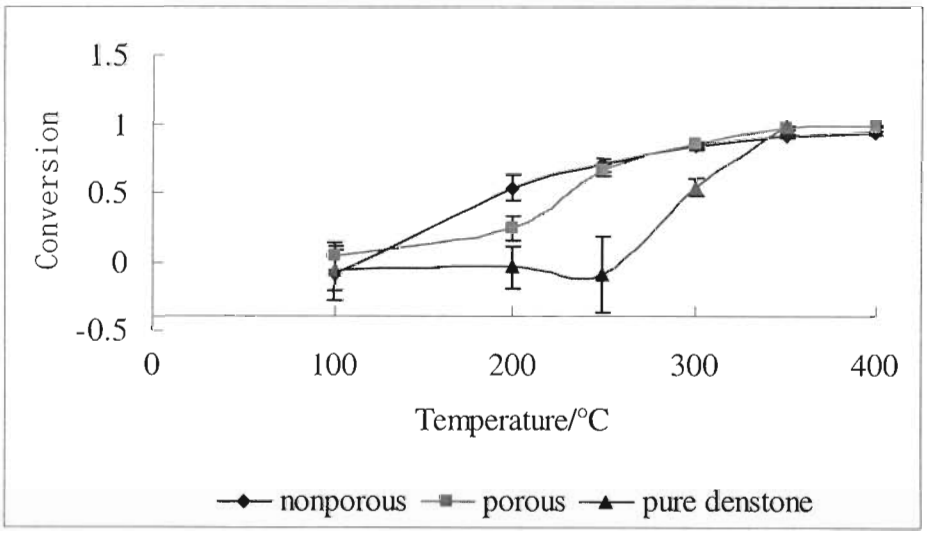

Figure 4.4. Comparison of 2-butanol conversion versus reaction temperature on nonporous WO_3/Al_2O_3, porous WO_3/Al_2O_3, and Al_2O_3 (pure Denstone support).

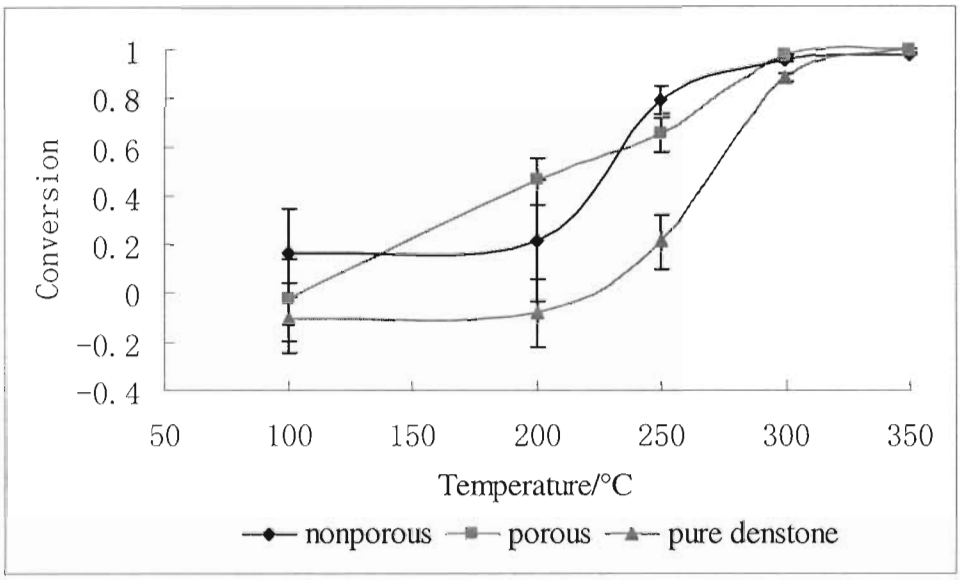

Figure 4.5. Comparison of 2-hexanol conversion versus reaction temperature on nonporous WO_3/Al_2O_3, porous WO_3/Al_2O_3, and Al_2O_3 (pure Denstone support).

4.4. Alcohol Oxidation

4.4.1. Methanol Oxidation

Dimethyl ether was reported to be the main product of methanol desorption on Al_2O_3 between 200 and 400°C[26, 49-52]. However, dimethyl ether was not detected in our experiments, which means that there must be some other products produced since the methanol conversion was high. We presume that CO or CO_2 were the main products; however, because these products elute with the air on the DB-1 column, the ionizer must be turned off to protect the filament and so these products could not be reliably confirmed (see section 3.7.4.). The presumption was made according to the following reasons: water flow in the gas stream introduced a substantial coverage of hydroxyls onto

the Al_2O_3 surface, which decreased the catalytic activity of Al_2O_3; high H_2O (gas) concentration also impeded the dimethyl ether formation from methanol which is thought to be a reversible reaction[51]. Typically, the catalytic activity of Al_2O_3 is not fully developed until it is pretreated to about 300-400°C[53] to dehydroxylate the surface. Our presumption is also consistent with the results of Cairati et al[54]., who reported that CO was the main product of methanol on Al_2O_3.

Previous work has demonstrated that methanol on WO_3/Al_2O_3 showed 100% selectivity to dimethyl ether, which was generally related to the acidic character of WO_3[26, 55]. There are two mechanisms[51] to interpret the formation of dimethly ether (see equation (2) and (3)): formation from two methoxy groups; and formation from molecularly adsorbed methanol and methoxy groups. Presently, it is still not clear which mechanism is right.

$$CH_3O^-(a) + CH_3O^-(a) \rightarrow CH3OCH_3(g) + O^{2-}(a) \quad (2)$$

$$CH_3OH(a) + CH_3O^-(a) \rightarrow CH_3OCH_3(g) + OH^-(a) \quad (3)$$

4.4.2. Ethanol Oxidation

Cordi et al.[52] reported that the dehydration product (ethylene) and dehydrogenation product (acetaldehyde) were formed when ethanol decomposed on Al_2O_3 by using temperature programmed desorption (TPD) and oxidation (TPO). The dehydration of ethanol was also studied as a model reaction to test the catalytic activity of different aluminas by Sivaraj et al[56]. In our experiments, only the dehydrogenation product

acetaldehyde was detected. However, we could not tell if there was ethylene produced because the retention time is not long enough (Kovats' retention index: 164 for DB-1 coloum[57]) to separate it from the air (see section 3.7.4). Trace amounts of acrolein were observed at 350°C, and its reaction mechanism might be a cross-aldol-condensation reaction between acetaldehyde and formaldehyde, where formaldehyde was formed by acetaldehyde oxidation[58-60].

Ethanol oxidation product distributions on WO_3/Al_2O_3, and Al_2O_3 were almost the same except for the presence of ethyl ether on WO_3/Al_2O_3 in the experiments at 250, 300, and 350°C, which was generally associated with the acidity of catalyst[61]. At 400°C, only acetaldehyde and acrolein were observed in the products. Our results of the ethanol oxidation on Al_2O_3 and WO_3/Al_2O_3 showed that the selective oxidation of ethanol on catalyst was strongly temperature related.

4.4.3. 2-propanol Oxidation

The study of Kulkarni et al.[27] showed that 2-propanol oxidation by Al_2O_3 produced propene and by WO_3 produced propene and isopropyl ether with the inlet gas ratio ~2:13:85 for $CH_3CH_2CHOH:O_2$:He, respectively. Small amounts of isopropyl ether were proposed to form via bimolecular recombination of surface isopropoxide species on acidic surface sites. The reaction is expressed with equation (4):

$$(CH_3)_2O^-(a) + (CH_3)_2O^-(a) \rightarrow (CH_3)_2O(CH_3)_2O(a) + O^{2-}(a) \qquad (4)$$

However, Gervasini et al.[62] showed different results for 2-propanol oxidation products on

Al_2O_3 and WO_3. In their research, the reactant was a mixture of 2-propanol in air, and the product distribution of 2-propanol on Al_2O_3 and WO_3 was the same, which included mainly propene and acetone (>95%), and traces of isopropyl ether (<1%). Although it is not clear why the product distribution on Al_2O_3 and WO_3 are different for the two experiments, the presence of H_2O in air is more likely to answer for the difference.

Our results (see Table 4.3.) showed that the 2-propanol oxidation products were mainly acetone and trace amounts of methyl vinyl ketone on both Al_2O_3 and WO_3/Al_2O_3 catalysts. Acetone was produced at 250, 300, 350 and 400°C; methyl vinyl ketone was observed in the higher temperature range from 300 to 400°C. The absence of isopropyl ether observed in our experiments was associated with the presence of O_2 which minimized the ether formation[63]. The absence of propene in the oxidation products should be associated with the substantial amounts of adsorbed water and hydroxyls on the catalyst surface introduced by the water vapor in the gas stream, which has been shown to increase the selectivity to acetone[63]. Formation of methyl vinyl ketone was thought to be a vapor phase aldol condensation reaction between acetone and formaldehyde[64, 65], and the potential pathway of the formation of formaldehyde might be acetone oxidation.

4.4.4. 2-butanol Oxidation

The studies of Macht et al.[28] and Baertsch et al.[66] showed that only dehydration of 2-butanol occurred on tungsten oxide catalysts at 200°C. The studies also showed that

the 2-butanol dehydration products were 1-butene, trans- and cis-2-butene, which are consistent with our results of 2-butanol oxidation on the WO_3/Al_2O_3 catalyst at low temperatures. At 100 and 200°C, the WO_3/Al_2O_3 catalyst only showed activity for 2-butanol dehydration to butenes. At high temperatures, both dehydration and dehydrogenation products were observed on these catalysts. The dehydration and dehydrogenation reactions are shown in equation (5) and (6):

$$CH_3CHOHC_2H_5 \rightarrow CH_3CH{=}CHCH_3 + H_2O \qquad (5)$$

$$CH_3CHOHC_2H_5 \rightarrow CH_3COC_2H_5 + H_2 \qquad (6)$$

Our results showed that the product distribution of 2-butanol on both Al_2O_3 and WO_3/Al_2O_3 were strongly affected by temperature. Trace amounts of isopropenyl methyl ketone were also detected during the experiments of 2-butanol on Al_2O_3 and WO_3/Al_2O_3 catalysts at 300 and 350°C. The mechanism of ketone formation is thought to be an aldol condensation reaction between 2-butanone and formaldehyde[67]. However, how the formaldehyde was produced in the ketone formation was still not fully understood.

4.4.5. 2-hexanol Oxidation

Our results (Table 4.5) showed that only dehydrogenation products of 2-hexanone were observed on the Al_2O_3 catalyst, which was different from the studies of Dirk et al.[68], where they reported dehydration products of 1-hexene, trans- and cis-2-hexene on alumina. The absence of dehydration products on Al_2O_3 was probably because of the water vapor on the Al_2O_3 surface which impeded the dehydration reaction.

On the WO_3/Al_2O_3 catalyst, only the dehydration products of trans- and cis-2-hexene were detected at 100°C. At higher temperatures, 1-hexene and 2-hexanone were also detected. By comparing the product distributions of 2-hexanol oxidation on Al_2O_3 and WO_3/Al_2O_3, we conclude that the WO_3 catalyst was active for 2-hexanol dehydration, but we could not tell if the WO_3 catalyst was active for 2-hexanol dehydrogenation because of the presence of Al_2O_3, which could result in dehydrogenation products.

4.5. The Effect of Water in Alcohols Oxidation on Catalysts

Our results of the alcohol product distribution on Al_2O_3 and WO_3 catalysts presented above showed some disagreements with the former studies, which were considered to be the effect of water in the alcohol reactions. Several examples of the effect of water in alcohol reactions on other metal oxides can also be found in the literature. Chadwick et al.[69] reported a significant influence of adsorbed water and hydroxyls on methanol oxidation on ZnO during temperature programmed desorption experiments. They found that the oxidation of methanol on dehydroxylated ZnO results in the formation of CO and H_2. When water was coadsorbed, CO_2 was observed in the product distribution; as the preadsorbed water was increased, the amount of CO formed decreased linearly, while the amount of CO_2 increased. The authors suggested that this change represents the opening of a new reaction channel to CO_2 formation as the surface hydroxyl concentration increases, probably through a direct reaction between adsorbed methoxy or a related intermediate and surface OH groups. Shido et al.[70] proposed a similar reaction

mechanism for the water-gas shift reaction over ZnO in which adsorbed CO reacts with surface hydroxyl groups to produce intermediate formate species. Rekoske et al.[63] reported that the presence of water, whether produced by 2-propanol dehydration or added independently, was found to increase the rate of 2-propanol dehydrogenation on oxidized anatase TiO_2. All of these studies and our results showed that water and/or surface hydroxyl groups play an important role in alcohols reaction on metal oxides.

4.6. Kinetic Analysis of 2-butanol Dehydration

Our results showed that alcohol conversion on Al_2O_3, porous and nonporous WO_3/Al_2O_3 increased with increasing reaction temperatures. Although the product distributions were not the same, both the Al_2O_3 and WO_3/Al_2O_3 catalysts were active to alcohol oxidation. According to our results, there was no conversion of methanol, ethanol and 2-propanol on both Al_2O_3 and WO_3/Al_2O_3 at 100 and 200°C, but the conversion of 2-butanol and 2-hexanol on WO_3/Al_2O_3 was observed at these temperatures which could be due to differences in the rate limiting step in primary versus secondary alcohols as well as higher surface residence times for the heavier alcohols.

Because of the contribution of the Denstone support media (Al_2O_3) to the alcohol oxidation, it was too hard to compare the catalytic activities of nonporous and porous WO_3. Accordingly, only limited information about the selectivity of porous WO_3 could be gained from our results. Combining the conversion curves and product distributions, only 2-butanol could be clearly identified to be nonactive to Al_2O_3 and active to WO_3 at

100 and 200°C. Also, Al_2O_3 did not show catalytic activity to 2-hexanol oxidation at 100°C but WO_3 did. Therefore, in order to compare the catalytic activity of nonporous and porous WO_3, only the conversion information of 2-butanol and 2-hexanol were valuable. Therefore, we restrict our analysis of the reaction kinetics on nonporous and porous WO_3 to the results of 2-butanol oxidation at 200°C.

The mechanism and apparent overall kinetics of 2-butanol dehydration and dehydrogenation have been previously described in detail using a so-called Langmuir-Hinshelwood (LH) mechanism[71-73], which is generally taken to separately describe the adsorption, surface reaction, and desorption steps. The basic idea of the LH mechanism is that all reactants are adsorbed prior to the actual reaction event. The LH mechanism is a sequence of reaction steps and each step is assumed to be an elementary step. Iglesia et.al[66] reported that the elementary steps of 2-butanol dehydration included the reversible nondissociative adsorption of 2-butanol on active sites, E2 elimination to form butene isomers, and H_2O desorption. The study of Iglesia et.al[66] also showed that the 2-butanol dehydration over WO_3 was a pseudo zero order reaction.

The dehydration rates of 2-butanol on nonporous and porous WO_3 powders at 200 °C were expressed by using turnover frequencies (TOF_w=molecules converted per second per gram WO_3; TOF_A=molecules converted per second per unit surface area) and listed in Table 4.6. For the same amount of catalyst, the surface area of porous WO_3 powder was about 3000 times of that of the nonporous WO_3. The TOF_w for porous WO_3 was only about 10 to 20 times of that of nonporous WO_3. Although the experimental

conditions were different for porous and nonporous WO_3, if the rate law is indeed zero order, then we would expect little change in the TOF_w ratio of porous WO_3 to nonporous WO_3. In any case, there was still a significant difference between the TOF_w ratio and surface area ratio (3000:1). The significant difference indicates that most of the surface of porous WO_3 powder was not active for 2-butanol dehydration. The comparison of TOF_A also indicates the low surface efficiency of porous WO_3. One explanation for these results could be associated with the pore size distribution of the porous WO_3. The exact pore size distribution of the porous WO_3 (A2 sample) was not shown in Waghe's[18] study. However, the sensor selectivity experiments in his study indicated that the pore size of the A2 sample was not big enough to allow the DMMP molecules to enter into the pores. The molecular size of DMMP (5.71 Å diameter) is similar to that of 2-butanol (5.38 Å diameter). Therefore, 2-butanol dehydration can only occur at the small external surface and not at the huge internal surface of the porous materials. Our results of 2-butanol dehydration on nonporous and porous WO_3 are clearly preliminary but are certainly consistent with the hypothesis of size selectivity based on the 2-butanol molecular size, proposed in Waghe's study[18] of the selectivity of porous WO_3 sensors.

Table 4.6. Reactivity of WO_3 catalysts toward 2-butanol oxidation

Catalyst			200°C			
	Weight (g)	Surface Area (m^2/g)	2-butanol in Loop (nmole)	2-butanol in Loop (nmole)	TOF_w ($\mu mol \cdot s^{-1} \cdot g^{-1}$)	TOF_A ($\mu mol \cdot s^{-1} \cdot m^{-2}$)
Nonporous WO_3	0.250	0.04	12.2	0.531±0.093	0.100±0.018	2.51±0.44
Porous WO_3	0.050	112	48.1	0.24±0.086	1.42±0.51	0.013±0.004

Chapter 5

SUMMARY AND FUTURE WORK

5.1. Summary of the Current Research Work

Our motivation was to study alcohol oxidation on nonporous WO_3 and porous WO_3 powders, which have well defined pore sizes and very large surface areas. We investigated the alcohol conversion and product distribution on both nonporous and porous powders on a Denstone support media using a new microreactor system based on a GC/MS. The kinetic data for 2-butanol oxidation on WO_3 was converted to approximate turnover frequencies (TOFs) so that a comparison could be made between the porous and nonporous materials.

5.1.1. Design of the Microreactor System

The alcohol partial pressure was maintained at a constant level by using a vapor liquid equilibrator (VLE), which was then diluted quantitatively using mass flow controllers in the gas delivery system. To make measurements of the conversion, the microreactor was configured between a pair of 2-position, 6-port valves to allow sampling of the gas upstream and downstream of the reactor. The upstream measurement was used to calculate the mass spectrometer response, while the downstream measurement yielded the concentration. Multiple measurements of the gas stream could be made using a 16 loop sampling valve.

The design of the microreactor allowed the reactor to be heated to the assigned temperature quickly due to the good heat conductivity of the brass collar. A unique factor of the design is that the internal reactor temperature could be measured through the reactor bed using a thermocouple which could be translated inside the thermowell. Reproducibility achieved for this system was about 6% (standard deviation of multiple variates), which was consistent with the calculated uncertainties. However, the 6% uncertainty resulted in the limitation of this system for measurements at low (<10%) conversion.

5.1.2. Alcohol Conversion and Product Distribution

Alcohol conversion on Al_2O_3, nonporous and porous WO_3/Al_2O_3 increased with the reactor temperature for all of the alcohols. For methanol, ethanol and 2-propanol, alcohol oxidation on Al_2O_3 and WO_3/Al_2O_3 occurred when the reactor temperature was higher than 200°C. For 2-butanol and 2-hexanol oxidation on WO_3/Al_2O_3, the onset of reaction occurred at a lower temperature of 100°C.

During the experiments of alcohol oxidation on Al_2O_3 and WO_3/Al_2O_3, both dehydration and dehydrogenation products were observed. According to the results of product distributions, Al_2O_3 and WO_3/Al_2O_3 showed the same catalytic activity only on 2-propanol oxidation. Some aldol condensation products were also detected in the experiments of ethanol on WO_3/Al_2O_3, 2-propanol on Al_2O_3 and WO_3/Al_2O_3, and 2-butanol on Al_2O_3, which was related to the water vapor in the overall stream.

5.1.3. Kinetic Analysis of 2-butanol Dehydration

The 2-butanol dehydration was analyzed using a Langmuir Hinshelwood mechanism. The rates of 2-butanol dehydration were reported as turnover rates (TOF_w, molecules converted per second per gram WO_3; and TOF_A, molecules converted per second per unit surface area). On the basis of surface area, a comparison of the TOF_A numbers for 2-butanol dehydration rates on nonporous and porous WO_3 indicated that the large internal surface area of the porous WO_3 showed little activity. This is in accordance with the size selectivity of porous WO_3 which was proposed in the previous study by Waghe[18].

5.2. Future Work

After the research work performed in this thesis, some work still needs to be conducted in order to further understand the alcohol oxidation product distributions and kinetics on the nonporous and porous WO_3 catalysts. Elimination of the catalytic activity of the Denstone support media is necessary; instrument method modifications are needed to confirm the complete oxidation product distribution and check the mass balance; further experiments are required to confirm the effect of water on alcohol dehydration.

5.2.1. Alcohols on WO_3 Catalyst with Inactive Support

The primary role of the Denstone support media was to preheat the reactant stream before reaching the WO_3 catalyst. However, our results showed that the support media

was active for alcohol oxidation, which prevented analysis of most of the data for the catalytic activities of nonporous and porous WO_3. New support media is therefore needed to replace the currently used Denstone support. The new support media must be inactive to alcohol oxidation. A former study[26] showed that the catalytic activity of SiO_2 to methanol oxidation could be neglected compared to that of WO_3, which means SiO_2 is a possible replacement for the Denstone support. However, to make sure that SiO_2 is an acceptable support in our experiments, evidence of the inactivity of SiO_2 to the other alcohols would need to be demonstrated using the blank experiments described in section 2.1.4.

5.2.2. GC/MS Instrument Method Modification

Because air comprised more than 99% in the total stream, and the retention time of air was about 2.6 minutes in the experiments, a 2.8 minute time delay was used to protect the filament of the ion source. The retention time of ethene was smaller than 2.8 minutes under the same operating conditions; therefore ethene might be missed in the MS spectra. To detect ethene in the ethanol oxidation products and also not damage the filament, the instrumentation method should be optimized. Within limits, the optimization can be reached by adjusting the tune setting delay time, lowering the initial oven temperature and increasing the split ratio.

The other disadvantage of the current instrument method is the type of column. By using a DB-1 column, it is too hard to separate CO and CO_2 from air. Since CO is a main

product of alcohol oxidation at high temperature, quantitative CO analysis is necessary in the alcohol kinetics calculations. To get the CO peak in the mass spectra, a secondary column must be prepared to separate CO from air. Generally, Porapak Q columns (*Agilent*) are applied to perform this separation.

5.2.3. Confirmation of the Effect of Water on Alcohol Oxidation

Our results showed some different product distributions compared to former studies. For example, no dimethyl ether was detected for methanol oxidation on Al_2O_3; no ethyl ether was detected for ethanol oxidation on Al_2O_3; no propene was detected for 2-propanol reaction on Al_2O_3 and WO_3/Al_2O_3, and some aldol condensation products were formed during the alcohol oxidation. All these disagreements were presumed to be related to the presence of water in the gas stream. Further experiments with different water vapor flow rates and without water vapor introduced into the reactant mixtures should be carried out to check the consistency of the products distributions in our current results and literatures.

5.2.4. Implication for Sensor Research

The new microreactor system based on a GC/MS is suitable to measure the catalytic activity of powder materials for a variety of gas reactants. Information of product distribution and conversion can extracted from the measurements. Our results also indicate that the effect of water in alcohol oxidation product distribution is substantial.

Only redox reactions should give a response in SMO sensors, so examination of the reaction products and conversion provides useful information regarding the sensitivity of the sensor to the target compound.

REFERENCES

1. Shimizu, Y.; Makoto, E., *MRS Bulletin* **1999,** 24, 18.
2. Morrison, S. R., *Journal of physical Chemistry* **1953,** 57, 860.
3. Brattain, W. H.; Bardeen, J., *The Bell System Technical Journal* **1953,** 32, 1.
4. Taguchi, N. U.S. Patent. 1971.
5. Taylor, S. H.; Hargreaves, J. S. J.; Hutchings, G. J.; Joyner, R. W., *Applied Catalysis, A: General* **1995,** 126, (2), 287-296.
6. Hutchings, G. J.; Taylor, S. H., *Catalysis Today* **1999,** 49, 105.
7. Moulzolf, S. C.; Frankel, D. J.; Lad, R. J., *Review of Scientific Instruments* **2002,** 73, (6), 2325-2330.
8. Solis, J. L.; Saukko, S.; Kish, L.; Granqvist, C. G.; Lantto, V., *Thin Solid Films* **2001,** 391, 255-260.
9. Lozzi, L.; Ottaviano, L.; Passacantando, M.; Santucci, S.; Cantalini, C., *Thin Solid Films* **2001,** 391, 224-228.
10. Moulzolf, S. C.; LeGore, L. J.; Lad, R. J.; *Thin Solid Films* **2001,** 56, *Thin Solid Films* **2001,** 400, (1-2), 56-63.
11. Pilling, R. S.; Bernhardt, G.; Kim, C. S.; Duncan, J.; Crothers, C. B. H.; Kleinschmidt, D.; Frankel, D. J.; Lad, R. J.; Frederick, B. G., *Sensors and Actuators, B: Chemical* **2003,** B96, (1-2), 200-214.
12. Bender, F.; Barie, N.; Romoudis, G.; Voigt, A.; Rapp, M., *Sens. Actuators B* **2003,** B 93(1-3), 135-141.
13. Mecklenburg, M.; Danielsson, B.; Winquist, F., *PCT Int. Appl.* **1997**, 29.
14. Williams, G.; Coles, G. S. V., *MRS Bulletin* **1999,** 24, 30.
15. Choi, Y.; Sakai, G.; Shimanoe, K.; Y.Teraoka; Miura, N.; Yanazoe, N., *Sensors and Actuators B: Chemical* **2003,** 95, (1-3), 258-265.
16. Martin, A. Master thesis. University of Maine, 2004.
17. Fruhberger, B.; Stirling, N.; Grillo, F. G.; Ma, S.; Ruthven, D.; Lad, R. J.; Frederick, B. G., *Sensors and Actuators B* **2001,** 76, (226).
18. Waghe, A. B. Ph.D. Thesis. University of Maine, Orono, 2003.
19. Ionescu, R.; Hoela, A.; Granqvist, C. G.; Llobet, E.; Heszler, P., *Sensors and Actuators B: Chemical* **2005,** 104, (1), 124-131.
20. Ionescu, R.; Llobet, E.; Brezmes, J.; Vilanova, X.; Correig, X., *Sensors and Actuators B: Chemical* **2003,** 95, (1-3), 177-182.

21. Pilling, R. S.; Kim, C. S.; Frederick, B. G., *Sensors and Actuators, B: Chemical* **2002,** unpublished.
22. Meixner, H.; Lampe, U., *Sens. Actuators B* **1996,** 33, 198.
23. Ma, S.; Frederick, B. G., *J. Phys. Chem* **2004,** unpublished.
24. Jones, F. H.; Dixon, R. A.; Brown, A., *Surface Science* **1996,** 369, 343.
25. Salje, E.; Carley, A. F.; Roberts, M. W., *J. Solid State Chem* **1979,** 29, 237.
26. Badlani, M.; Wachs, I. E., *Catalysis Letters* **2001,** 75, (3-4), 137-149.
27. Kulkarni, D.; Wachs, I. E., *Applied Catalysis A: General* **2002,** 237, 121-137.
28. Macht, J.; Baertsch, C. D.; May-Lozano, M.; Soled, S. L.; Wang, Y.; Iglesia, E., *Journal of catalysis* **2004,** 227, 479-491.
29. Tatibouët, J. M., *Applied Catalysis A: General* **1997,** 148, 213-252.
30. Ma, S.; Amar, F. G.; Frederick, B. G., *Journal of Physical Chemistry A* **2003,** 107, (9), 1413-1423.
31. Ma, S.; Frederick, B. G., *Journal of Physical Chemistry B* **2003,** 107, (43), 11960-11969.
32. Bernhardt, G.; Silvestre, C.; LeCursi, N.; Moulzolf, S. C.; Frankel, D. J.; Lad, R. J., *Sens. Actuators B* **2001,** 77, 368.
33. Lu, Z.; Kanan, S. M.; Cox, J.; Tripp, C. P., *Chem. Mater.* **2002,** 12, 983.
34. Kanan, S. M.; Lu, Z.; Cox, J. K.; Bernhardt, G.; Tripp, C. P., *Langmuir* **2002,** 18, 1707.
35. Kanan, S. M.; Lu, Z.; Tripp, C. P., *J. Phys. Chem. B* **2002,** 106, 9576.
36. Kanan, S. M.; Tripp, C. P., *Langmuir* **2002,** 18, 722.
37. Kim, C. S.; Lad, R. J.; Tripp, C. P., *Sensors and Actuators B* **2001,** 76, 442.
38. Thomas, J. M.; Thomas, W. J., *Principles and Practice of Heterogeneous Catalysis*.VCH: New York, 1997.
39. Burcham, L. J.; Badlani, M.; Wachs, I. E., *Journal of Catalysis* **2001,** 203, 104-121.
40. http://webbook.nist.gov/chemistry/.
41. Fogler, H. S., *Elements Of Chemical Reaction Engineering*. 4th ed.; Prentice Hall: 2005.
42. Bird, R. B.; Stewart, W. E.; Lightfoot, E. N., *Transport Phenomena*. Wiley: New York, 1960.
43. Levine, I. N., *Physical Chemistry*. 5th ed.; McGraw-Hill Companies: 2001.
44. Deemter, J. J. v.; Zuiderweg, F. F.; Klinkenberg, A., *Chem. Eng. Sci.* **1956,** 5, 271-289.
45. Desty, D. H.; Gouldup, A.; Whyman, B. H. F., *J. Inst. Petrol* **1959,** 45, 287-298.
46. Technologies, A., Carrier Gases in Capillary GC Analysis, http://www.chem.agilent.com/temp/rad24819/00047438.pdf.

47. Bielański, A.; Haber, J., *Oxygen in catalysis*. Marcel Dekker, Inc.: 1991.
48. Ai, M., *Journal of catalysis* **1978,** 54, 426-435.
49. Burcham, L. J.; Briand, L. E.; Wachs, I. E., *Langmuir* **2001,** 17, 6175-6184.
50. Briand, L. E.; Hirt, A. M.; Wachs, I. E., *Journal of catalysis* **2001,** 202, 268-278.
51. Schiffino, R. S.; Merrill, R. P., *Journal of physical Chemistry* **1993,** 97, 6425-6435.
52. Cordi, E. M.; Falconer, J. L., *Journal of catalysis* **1996,** 162, 104-117.
53. Knözinger, H.; Ratnasmy, P., *P. Catal. Rev.-Sci. Eng.* **1978,** 17, (1), 31.
54. Cairati, L.; Trifiro, F., *Journal of catalysis* **1983,** 80, 25.
55. Vergnon, P.; Tatibouët, J. M., *Bull. Soc. Chem. Fr.* **1980,** 11-12, 455.
56. Sivaraj, C.; Reddy, B. P.; Rao, B. R.; Rao, P. K., *Applied Catalysis* **1986,** 24, 25-35.
57. Hoekman, S. K., *J. Chromatogr.* **1993,** 639, 239-253.
58. Zhao, Z.; Yamada, Y.; Teng, Y.; Ueda, A.; Nakagawa, K.; Kobayashi, T., *Journal of catalysis* **2000,** 190, (2), 215-227.
59. Ai, M., *Bull. Chem. Soc. Jpn.* **1991,** 64, 1346.
60. Dumitriu, E.; Hulea, V.; Chelaru, C.; Catrinescu, C.; Tichit, D.; Durand, R., *Appl. Catal.A* **1999,** 178, 145.
61. Borsa, T. K.-. Cowley, S. W., *American Chemical Society, Division of Fuel Chemistry* **2004,** 49, (2), 856-859.
62. Gervasini, A.; Auroux, A., *Journal of catalysis* **1991,** 131, 190-198.
63. Rekoske, J. E.; Barteau, M. A., *Journal of catalysis* **1997,** 165, 57.
64. Ai, M., *Journal of catalysis* **1987,** 106, 273-279.
65. Tanner, R.; Gill, P.; Wells, R.; Bailie, J. E.; Kelly, G.; Jackson, S. D.; Hutchings, G. J., *Phys. Chem. Chem. Phys.* **2002,** 4, 688-695.
66. Baertsch, C. D.; Komala, K. T.; Chua, Y.-H.; Iglesia, E., *Journal of catalysis* **2002,** 205, 44-577.
67. Landau, E. F.; Irany, E. P., *Journal of Organic Chemistry* **1947,** 12, 422-425.
68. Dirk, D.; Helmut., K., *Journal of Catalysis* **1974,** 33, (1), 142-144.
69. Chadwick, D.; Zheng, K., *Catalysis Letters* **1993,** 20, 231.
70. Shido, T.; Iwasawa, Y., *Journal of catalysis* **1991,** 129, 343.
71. Jacobs, P. A.; Tielen, M.; Uytterhoeven, J. B., *Journal of catalysis* **1977,** 50, (1), 98-108.
72. Hajek, M.; Duchet, J. C.; Kockloefl, K., *Collection of Czechoslovak Chemical Communications* **1970,** 35, (8), 2258-2274.
73. Gulková, D.; KrausMilo, M., *Journal of Molecular Catalysis* **1994,** 87, (1), 47-55.

APPENDICES

Appendix A. METHANOL CONCENTRATION AND UNCERTAINTY CALCULATIONS

Initial parameters

Temperature of VLE: $Tvle := (273 + 20)K$

Temperature of reactor: $Treactor := (273 + 20)K$

Pressure parameters: $P1 := 12psi$ $P2 := 12.5psi$

$P3 := 10.6psi$ $P4 := 5.28psi$

Flow rate: $F1 := 40\frac{cm^3}{min}$ $F2 := 5\frac{cm^3}{min}$ $F3 := 200\frac{cm^3}{min}$

Sampling Loop Property

Loop temperature: $Tloop := (21 + 273.15)K$

Loop volume: $Vloop := 0.75cm^3$

Temperature uncertainty: $\sigma Tloop := 2.2K$

Loop volume uncertainty: $\sigma Vloop := 0.02cm^3$

Calibrated parameters

Calibrated pressure parameters:

$P1c := 1.0722 \cdot P1 + 0.10098psi$ $P2c := 1.0385 \cdot P2 - 0.034615psi$

uncertiatny : 0.0206 0.19 0.037 0.355

$P3c := 0.9537 \cdot P3 + 0.79815psi$ $P4c := P4$

uncertiatny : 0.016 0.155

Calibrated flow rate:

$$F1c := 1.0881 \cdot F1 - 1.8147 \frac{cm^3}{min} \qquad F1c = 41.709 \frac{cm^3}{min}$$

uncertainty : 0.00541 0.328

$$F2c := 2.153 \cdot F2 - 2.0381 \frac{cm^3}{min} \qquad F2c = 8.727 \frac{cm^3}{min}$$

uncertainty : 0.0105 0.0676

$$F3c := 1.1243 \cdot F3 - 0.075773 \frac{cm^3}{min} \qquad F3c = 224.784 \frac{cm^3}{min}$$

uncertainty : 0.000993 0.0634

Uncertainty of Pressure Temperature and flow rate:

$$\sigma P1 := \left[P1^2 \cdot 0.0206^2 + 1.0722^2 \cdot (0.15psi)^2 + (0.19 \cdot psi)^2 \right]^{\frac{1}{2}} \qquad \sigma P1 = 0.351\,psi$$

$$\sigma P2 := \left[P2^2 \cdot 0.037^2 + 1.0385^2 \cdot (0.15psi)^2 + (0.355 \cdot psi)^2 \right]^{\frac{1}{2}} \qquad \sigma P2 = 0.603\,psi$$

$$\sigma P3 := \left[P3^2 \cdot 0.016^2 + 0.9537^2 \cdot (0.15psi)^2 + (0.155 \cdot psi)^2 \right]^{\frac{1}{2}} \qquad \sigma P3 = 0.271\,psi$$

$$\sigma P4 := 0.035psi$$

$$\sigma F1c := \left[F1^2 \cdot 0.00541^2 + 1.0881^2 \cdot \left(0.5 \frac{cm^3}{min} \right)^2 + \left(0.328 \cdot \frac{cm^3}{min} \right)^2 \right]^{\frac{1}{2}} \qquad \sigma F1c = 0.671 \frac{cm^3}{min}$$

$$\sigma F2c := \left[F2^2 \cdot 0.0105^2 + 2.153^2 \cdot \left(0.1 \frac{cm^3}{min} \right)^2 + \left(0.0676 \cdot \frac{cm^3}{min} \right)^2 \right]^{\frac{1}{2}} \qquad \sigma F2c = 0.232 \frac{cm^3}{min}$$

$$\sigma F3c := \left[F3^2 \cdot 0.000993^2 + 1.1243^2 \cdot \left(0.5 \frac{cm^3}{min} \right)^2 + \left(0.0634 \cdot \frac{cm^3}{min} \right)^2 \right]^{\frac{1}{2}} \qquad \sigma F3c = 0.6 \frac{cm^3}{min}$$

Uncertainty of VLE temperature:

$$\sigma T := 2.2K$$

Antoine equation coefficients:

For methanol:

$$A1 := 8.08097 \qquad B1 := 1582.271 \qquad C1 := 239.726$$

For water:

$$A2 := 8.07131 \qquad B2 := 1730.630 \qquad C2 := 233.426$$

Uncertainties of these coefficients:

$$\sigma A1 := 0.00001 \qquad \sigma B1 := 0.001 \qquad \sigma C1 := 0.001$$

$$\sigma A2 := 0.00001 \qquad \sigma B2 := 0.001 \qquad \sigma C2 := 0.001$$

Partial pressure of MeOH and H_2O in VLEs:

$$Pm(Tvle) := 10^{\left(A1 - \left(\frac{B1}{C1 - 273.15 + \frac{Tvle}{K}}\right)\right)} \cdot torr \qquad Pm(Tvle) = 96.688\,torr$$

$$Ph(Tvle) := 10^{\left(A2 - \frac{B2}{C2 - 273.15 + \frac{Tvle}{K}}\right)} \cdot torr \qquad Ph(Tvle) = 17.311\,torr$$

Uncertainty of Partial pressure of MeOH and H_2O:

For MeOH

$$\sigma Pm1 := \sigma A1^2 \cdot \left(\frac{Pm(Tvle)}{torr}\right)^2 \qquad \sigma Pm2 := \frac{\sigma B1^2 \cdot \left(\frac{Pm(Tvle)}{torr}\right)^2}{\left(\frac{Tvle}{K} - 273.15 + C1\right)^2}$$

$$\sigma Pm3 := \frac{\sigma C1^2 \cdot B1^2 \cdot \left(\frac{Pm(Tvle)}{torr}\right)^2}{\left(\frac{Tvle}{K} - 273.15 + C1\right)^4} \qquad \sigma Pm4 := \frac{\left(\frac{\sigma T}{K}\right)^2 \cdot B1^2 \cdot \left(\frac{Pm(Tvle)}{torr}\right)^2}{\left(\frac{Tvle}{K} - 273.15 + C1\right)^4}$$

$$\sigma Pm := \left(\sigma Pm1 + \sigma Pm2 + \sigma Pm3 + \sigma Pm4\right)^{\frac{1}{2}} \cdot torr \qquad \sigma Pm = 4.995\,torr$$

For H_2O

$$\sigma Ph1 := \sigma A2^2 \cdot \left(\frac{Ph(Tvle)}{torr} \right)^2 \qquad \sigma Ph2 := \frac{\sigma B2^2 \cdot \left(\frac{Ph(Tvle)}{torr} \right)^2}{\left(\frac{Tvle}{K} - 273.15 + C2 \right)^2}$$

$$\sigma Ph3 := \frac{\sigma C2^2 \cdot B2^2 \cdot \left(\frac{Ph(Tvle)}{torr} \right)^2}{\left(\frac{Tvle}{K} - 273.15 + C2 \right)^4} \qquad \sigma Ph4 := \frac{\left(\frac{\sigma T}{K} \right)^2 \cdot B2^2 \cdot \left(\frac{Ph(Tvle)}{torr} \right)^2}{\left(\frac{Tvle}{K} - 273.15 + C2 \right)^4}$$

$$\sigma Ph := \left(\sigma Ph1 + \sigma Ph2 + \sigma Ph3 + \sigma Ph4 \right)^{\frac{1}{2}} \cdot torr$$

$$\sigma Ph = 1.027\, torr$$

Mole fraction calcualtion

Mole fraction of MeOH and H2O in VLE:

$$Xmeohvle := \frac{Pm(Tvle)}{14.7psi + P2c} \qquad Xmeohvle = 0.068$$

$$Xh2Ovle := \frac{Ph(Tvle)}{14.7psi + P1c} \qquad Xh2Ovle = 0.012$$

Uncertainty of Mole fraction of MeOH and H2O in VLE:

$$\sigma Xmeohvle := \left[\frac{1}{\left(14.7 + \frac{P2c}{psi} \right)^2} \cdot \left(\frac{\sigma Pm}{psi} \right)^2 + \frac{\left(\frac{Pm(Tvle)}{psi} \right)^2}{\left(14.7 + \frac{P2c}{psi} \right)^4} \cdot \left(\frac{\sigma P2}{psi} \right)^2 \right]^{\frac{1}{2}}$$

$$\sigma Xmeohvle = 3.793 \times 10^{-3} \qquad \frac{\sigma Xmeohvle}{Xmeohvle} = 0.056$$

$$\sigma Xh2Ovle := \left[\frac{1}{\left(14.7 + \frac{P1c}{psi}\right)^2} \cdot \left(\frac{\sigma Ph}{torr}\right)^2 \cdot 0.0193368^2 + \frac{\left(\frac{Ph(Tvle)}{torr}\right)^2 \cdot 0.0193368^2}{\left(14.7 + \frac{P1c}{psi}\right)^4} \cdot \left(\frac{\sigma P1}{psi}\right)^2 \right]^{\frac{1}{2}}$$

$$\sigma Xh2Ovle = 7.343 \times 10^{-4} \qquad \frac{\sigma Xh2Ovle}{Xh2Ovle} = 0.061$$

MeOH and H2O flow from VLE:

$$Fmeoh := \frac{XmeohvleF2c}{1 - Xmeohvle} \qquad Fh2O := \frac{Xh2OvleF1c}{1 - Xh2Ovle}$$

$$Fmeoh = 0.633 \frac{cm^3}{min} \qquad Fh2O = 0.511 \frac{cm^3}{min}$$

Total flow and uncertainty from VLE's:

$$Fvleh2O := \frac{F1c}{1 - Xh2Ovle} \qquad Fvlemeoh := \frac{F2c}{1 - Xmeohvle}$$

$$Fvleh2O = 42.22 \frac{cm^3}{min} \qquad Fvlemeoh = 9.36 \frac{cm^3}{min}$$

$$\sigma Fvlemeoh := \left[\frac{1}{(1 - Xmeohvle)^2} \cdot \left(\frac{\sigma F2c}{\frac{cm^3}{min}}\right)^2 + \frac{\left(\frac{F2c}{\frac{cm^3}{min}}\right)^2}{(1 - Xmeohvle)^4} \cdot \sigma Xmeohvle^2 \right]^{\frac{1}{2}} \cdot \frac{cm^3}{min}$$

$$\sigma Fvleh2O := \left[\frac{1}{(1 - Xh2Ovle)^2} \cdot \left(\frac{\sigma F1c}{\frac{cm^3}{min}} \right)^2 + \frac{\left(\frac{F1c}{\frac{cm^3}{min}} \right)^2}{(1 - Xmeohvle)^4} \cdot \sigma Xh2Ovle^2 \right]^{\frac{1}{2}} \cdot \frac{cm^3}{min}$$

$$\sigma Fvlemeoh = 0.251 \frac{cm^3}{min} \qquad \sigma Fvleh2O = 0.68 \frac{cm^3}{min}$$

$$\frac{\sigma Fvlemeoh}{Fvlemeoh} = 0.027 \qquad \frac{\sigma Fvleh2O}{Fvleh2O} = 0.016$$

Uncertainty for MeOH and H_2O flow from VLE:

$$\sigma Fmeoh := \left(Fvlemeoh^2 \cdot \sigma Xmeohvle^2 + Xmeohvle^2 \cdot \sigma Fvlemeoh^2 \right)^{\frac{1}{2}}$$

$$\sigma Fh2O := \left(Fvleh2O^2 \cdot \sigma Xh2Ovle^2 + Xh2Ovle^2 \cdot \sigma Fvleh2O^2 \right)^{\frac{1}{2}}$$

$$\sigma Fmeoh = 0.039 \frac{cm^3}{min} \qquad \sigma Fh2O = 0.032 \frac{cm^3}{min}$$

Methanol in overall stream:

$$Ftotal := F3c + Fvlemeoh + Fvleh2C \qquad Ftotal = 276.364 \frac{cm^3}{min}$$

$$\sigma Ftotal := \left(\sigma Fmeoh^2 + \sigma Fh2O^2 + \sigma F1c^2 \right)^{\frac{1}{2}} \qquad \sigma Ftotal = 0.673 \frac{cm^3}{min}$$

MeOH mole fraction in overall stream:

$$Xmeoh := \frac{Fmeoh}{Ftotal} \qquad Xmeoh = 2.29 \times 10^{-3}$$

Uncertainty of the mole fraction

$$\sigma Xmeoh := \left(\frac{1}{Ftotal^2} \cdot \sigma Fmeoh^2 + \frac{Fmeoh^2}{Ftotal^4} \cdot \sigma Ftotal^2 \right)^{\frac{1}{2}}$$

$$\sigma Xmeoh = 1.425 \times 10^{-4}$$

Relative uncertainty:

$$\sigma relative := \frac{\sigma Xmeoh}{Xmeoh} \qquad \sigma relative = 0.062$$

Methanol in Sampling loop

Loop capacity: (mole)

$$Cap := \frac{Vloop}{Tloop} \cdot \frac{14.7 \cdot psi + P4c}{0.0821 \cdot L \cdot atm \cdot mol^{-1} \cdot K^{-1}} \qquad Cap = 4.222 \times 10^{-5}\ mol$$

$$\sigma Cap := Cap \cdot \left[\frac{\sigma Vloop^2}{Vloop^2} + \frac{\sigma P4^2}{(14.7psi + P4c)^2} + \frac{\sigma Tloop^2}{Tloop^2} \right]^{\frac{1}{2}}$$

$$\sigma Cap = 1.172 \times 10^{-6}\ mol \qquad \frac{\sigma Cap}{Cap} = 0.028$$

Methanol in loop:

$$Cmeoh := Cap \cdot Xmeoh \qquad Cmeoh = 9.67 \times 10^{-8}\ mol$$

Uncertainty of methanol in loop:

$$\sigma := Cmeoh \cdot \left(\frac{\sigma Cap^2}{Cap^2} + \frac{\sigma Xmeoh^2}{Xmeoh^2} \right)^{\frac{1}{2}} \qquad \sigma = 6.589 \times 10^{-9}\ mol$$

Relative uncertainty of methanol concentration in loop:

$$\sigma L := \frac{\sigma}{Cmeoh} \qquad \sigma L = 0.068$$

APPENDIX B. ANTOINE EQUATION COEFFICIENTS

Antoine equation: $LogP = A - \frac{B}{T + C}$

P: partial pressure, (torr)

T: temperature, (°C)

A, B, and C: Antoine equation coefficients

	A	B	C
H_2O [1]	8.07131	1730.630	233.426
Methanol [1]	8.08097	1582.271	239.726
Ethanol [1]	8.11220	1592.864	226.184
2-propanol [1]	8.87829	2010.330	252.636
2-butanol [1]	7.47429	1314.188	186.500
2-hexanol [2]	6.51932*	2076.433*	-36.261*

*: The coefficients are corresponding to the Antoine equation with different units setting (P / bar, T / K).

[1] Gmehling, Jürgen, **Vapor-liquid equilibrium data collection**, Chemistry data series; v. 1, pt. 1; v. 1, pt. 2a, Frankfurt, 1977

[2] Hovorka, F.; Lankblma, H.P.; Stanford, S.C., **J. Am. Chem. Soc.**, 1938, 60, 820-827

APPENDIX C: MICROREACTOR BED PRESSURE DROP CALCULATION

$R := 8.314 \cdot \frac{joule}{K \cdot mole}$ $\quad \mu poise := 10^{-6} \cdot poise$ $\quad \mu m := 10^{-6} \cdot m$

$centipoise := 10^{-2} \cdot poise$

Calculation of Viscosity of Air as a function of temperature:

$T := 150 \cdot K, 155 \cdot K .. 1500 \cdot K$

From Carl L. Yaws, Chemical Properties Handbook, for air:

$A := 42.606 \cdot \mu poise$ $\quad B := 0.475 \cdot \frac{\mu poise}{K}$ $\quad C := -9.88 \cdot 10^{-5} \cdot \frac{\mu poise}{K^2}$

$\eta(T) := A + B \cdot T + C \cdot T^2$ (micropoise)

$\eta(150 \cdot K) = 1.116 \times 10^{-5}\ kg \cdot m^{-1} \cdot s^{-1}$ $\quad \eta(300 \cdot K) = 1.762 \times 10^{-5}\ kg \cdot m^{-1} \cdot s^{-1}$

$\eta(1500 \cdot K) = 5.328 \times 10^{-5}\ kg \cdot m^{-1} \cdot s^{-1}$

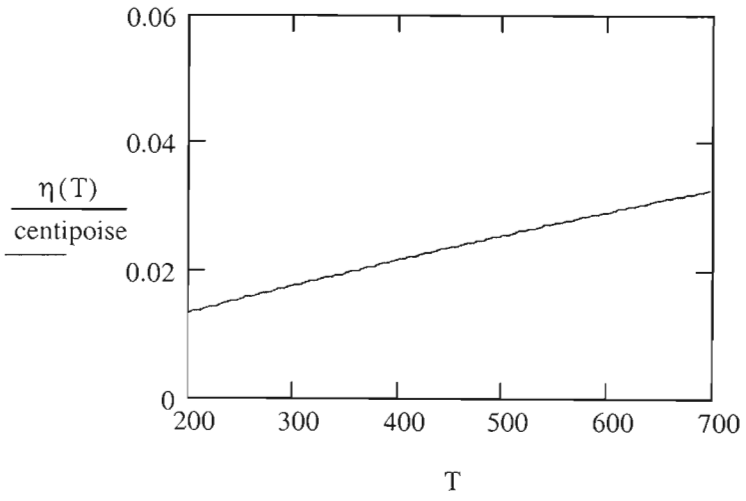

Calculate the pressure drop through the reactor.

$$flow := 250 \cdot \frac{cm^3}{60 \cdot sec}$$ sccm of air at room temperature

The cross sectional area in the microreactor is the annulus between the thermowell tube and the ID of the 1/4" s.s. tube:

$$Area := \left[\pi \cdot \left(\frac{0.25 \cdot in - 2 \cdot .020 \cdot in}{2} \right)^2 - \pi \cdot \left(\frac{0.0625 \cdot in}{2} \right)^2 \right] \qquad Area = 0.204\,cm^2$$

Superficial velocity:

$$u := \frac{flow}{Area} \qquad u = 0.205 \frac{m}{sec} \qquad 0.25 \cdot in - .035 \cdot in = 0.215\,in$$

Molecular weight of air:

$$Mw := (28 \cdot 0.8 + 32 \cdot 0.2) \cdot \frac{gm}{mole} \qquad Mw = 28.8 \frac{gm}{mole}$$

Initial pressure at head of reactor, at room temperature (P3)

$$P0 := \frac{14.7 + 12}{14.7} \cdot atm \qquad T0 := 298 \cdot K$$

initial gas density at room temperature:

$$\rho 0(T0, P0) := \frac{Mw \cdot P0}{R \cdot T0} \qquad \rho 0(T0, P0) = 0.134 \frac{lb}{ft^3}$$

superficial mass velocity:

$$G(P0, T) := u \cdot \rho 0(T, P0) \qquad G[P0, (320 + 273) \cdot K] = 0.022 \frac{gm}{cm^2 \cdot sec}$$

$$g_c := 1$$

$$\beta(T,P0,\phi,Dp) := \frac{G(P0,T)\cdot(1-\phi)\cdot\left[150\cdot(1-\phi)\cdot\frac{\eta(T)}{Dp}+1.75\cdot G(P0,T)\right]}{\rho0(T0,P0)\cdot Dp\cdot\phi^3}$$

$$\beta\left(298\cdot K,1\cdot atm,0.4,2\cdot10^{-5}\cdot m\right) = 75.095\,\frac{atm}{m}$$

$$PD(T,P0,\phi,Dp,z) := \left(1-\sqrt{1-2\cdot\frac{\beta(T,P0,\phi,Dp)}{P0}\cdot z}\right)\cdot P0$$

For methanol sampling downstream, P3 = 9.8 psig, and T = 300K

$T_{rxn} := (300 + 273)\cdot K$

$P3 := \frac{9.8 + 14.7}{14.7}\cdot atm$ $\quad P3 = 1.667\,atm$

$\rho_{Denstone} := \frac{115\cdot\frac{lb}{ft^3}}{1-0.4}$ $\quad \rho_{WO3} := 7.16\cdot\frac{gm}{cm^3}$

$\rho_{Denstone} = 3.07\,\frac{gm}{cm^3}$

$\phi := 0.4$ volume of void/volume of bed

$Length(mass,\phi,\rho solid) := \frac{mass}{\rho solid\cdot Area\cdot(1-\phi)}$

$Length\left(2.5\cdot gm,\phi,\rho_{Denstone}\right) = 2.623\,in$

$\phi := 0.4$ $\quad \phi := 0.35$

2.62 in $\quad$ 2.422 in $\quad$ length decreased 7.6%

Estimate maximum drop across first Denstone layer if the temperature immediately equilibrated to the reactor temperature:

$$PD\left(T_{rxn}, P3, \phi, 567.5 \cdot \mu m, Length\left(2.5 \cdot gm, \phi, \rho_{Denstone}\right)\right) = 0.082\,psi$$

$$P_1 := P3 - PD\left(T_{rxn}, P3, \phi, 567.5 \cdot \mu m, Length\left(2.5 \cdot gm, \phi, \rho_{Denstone}\right)\right)$$

$$P_1 = 1.661\,atm$$

$$P_2 := P3 - PD\left(T_{rxn}, P_1, \phi, 20 \cdot \mu m, Length\left(0.25 \cdot gm, \phi, \rho_{WO3}\right)\right)$$

$$P_2 = 1.477\,atm$$

$$P_3 := P_2 - PD\left(T_{rxn}, P_2, \phi, 135 \cdot \mu m, Length\left(0.25 \cdot gm, \phi, \rho_{Denstone}\right)\right)$$

$$P_3 = 1.467\,atm$$

$$P_4 := P_3 - PD\left(T_{rxn}, P_3, \phi, 302.5 \cdot \mu m, Length\left(.5 \cdot gm, \phi, \rho_{Denstone}\right)\right)$$

$$P_4 = 1.463\,atm$$

$$P_5 := P_4 - PD\left(T_{rxn}, P_4, \phi, 567 \cdot \mu m, Length\left(1.5 \cdot gm, \phi, \rho_{Denstone}\right)\right)$$

$$P_5 = 1.46\,atm$$

Total drop in pressure across bed: $P3 - P_5 = 3.035\,psi$

When f=0.35, the total drop in pressure across bed is 5.104 psi, which is 168% of the pressure drop with f=0.4

BIOGRAPHY OF THE AUTHOR

Meng Lu was born in Heze, Shandong Province, P.R. China on March 7th, 1978. He graduated from the First High School of Dingtao in Shandong Province in 1995. He attended the Tianjin University and graduated in 1999 with a Bachelor's degree in Chemical Engineering. After he worked in Tianjin Lishen Battery Joint-Stock Co., Ltd, Meng Lu began his graduate study at the University of Maine, Orono, Maine, in 2001. Meng Lu is a candidate for the Master of Science degree in Chemistry from The University of Maine in December, 2005.